OXFORD

Journal of Petrology, 2022, **63**, 1–25
https://doi.org/10.1093/petrology/egac040
Advance access publication date 29 April 2022
Original Manuscript

Oceanic Zircon Records Extreme Fractional Crystallization of MORB to Rhyolite on the Alarcon Rise Mid-Ocean Ridge

Ryan Portner[1,3,*], Brian M. Dreyer[2], David A. Clague[3], Nathan R. Daczko[4] and Paterno R. Castillo[5]

[1]Geology Department, San Jose State University, San Jose, CA 95192, USA
[2]Department of Earth and Planetary Sciences, University of California Santa Cruz, Santa Cruz, CA 95064, USA
[3]Monterey Bay Aquarium Research Institute, Moss Landing, CA 95039, USA
[4]Australian Research Council (ARC) Centre of Excellence for Core to Crust Fluid Systems and GEMOC, Department of Earth and Environmental Sciences, Macquarie University, Sydney, New South Wales 2109, Australia
[5]Scripps Institution of Oceanography, University of California, San Diego, La Jolla, CA 92093-0212, USA

*Corresponding author: E-mail: ryan.portner@sjsu.edu

Abstract

The first known occurrence of rhyolite along the submarine segments of the mid-ocean ridge (MOR) system was discovered on Alarcon Rise, the northernmost segment of the East Pacific Rise (EPR), by the Monterey Bay Aquarium Research Institute in 2012. Zircon trace element and Hf and O isotope patterns indicate that the rhyolite formed by extreme crystal fractionation of primary mid-ocean ridge basalt (MORB) sourced from normal to enriched MOR mantle with little to no addition of continental lithosphere or hydrated oceanic crust. A large range in zircon εHf spanning 11 ε units is comparable to the range of whole rock εHf from the entire EPR. This variability is comparable to continental granitoids that develop over long periods of time from multiple sources. Zircon geochronology from Alarcon Rise suggests that at least 20 kyr was needed for rhyolite petrogenesis. Grain-scale textural discontinuities and trace element trends from zircon cores and rims are consistent with crystal fractionation from a MORB magma with possible perturbations associated with mixing or replenishment events. Comparison of whole rock and zircon oxygen isotopes with modeled fractionation and zircon-melt patterns suggests that, after they formed, rhyolite magmas entrained hydrated mafic crust from conduit walls during ascent and/or were hydrated by seawater in the vent during eruption. These data do not support a model where rhyolites formed directly from partial melts of hydrated oceanic crust or do they require assimilation of such crust during fractional crystallization, both models being commonly invoked for the formation of oceanic plagiogranites and dacites. A spatial association of highly evolved lavas (rhyolites) with an increased number of fault scarps on the northern Alarcon Rise might suggest that low magma flux for ~20 kyr facilitated extended magma residence necessary to generate rhyolite from MORB.

INTRODUCTION

Evolved lavas on the mid-ocean ridge (MOR) system are extremely rare (Fig. 1A). Until recently (Clague *et al.*, 2018), rhyolite had only been observed in thick oceanic crust of hot-spot affected segments such as Iceland and the Galapagos (Geist *et al.*, 1995; Haase *et al.*, 2005; Bindeman *et al.*, 2012*a*). 'Normal' oceanic crust generated along the submerged MOR system does contain a minor component of evolved plutonic rocks, most having been sampled from plutonic sections of drill holes, exhumed footwalls of oceanic core complexes and ophiolites (e.g. Sharapov *et al.*, 2013; Grimes *et al.*, 2015; Padilla *et al.*, 2016). Moreover, dacite, andesite, and basaltic andesite make up an exceedingly small component of normal thickness MORs (e.g. Haase *et al.*, 2005; Wanless *et al.*, 2010). The discovery of a rhyolite lava dome with up to 77 wt% SiO_2 on the Alarcon Rise segment of the East Pacific Rise (EPR) in the Gulf of California (Fig. 1B) is the first of its kind identified on the global submarine MOR system (Clague *et al.*, 2018), and its source and petrogenesis are the focus of this study.

The genesis and eruption of rare evolved lavas on the largely basalt-covered MOR system remain enigmatic because extensive magmatic differentiation should be limited by voluminous decompression melting of the Earth's mantle and robust magma resupply rates. The latter limits the extent for cooling and crystal fractionation to progress prior to eruption (Christie &

Received: May 30, 2021. **Revised:** April 5, 2022. **Accepted:** April 20, 2022

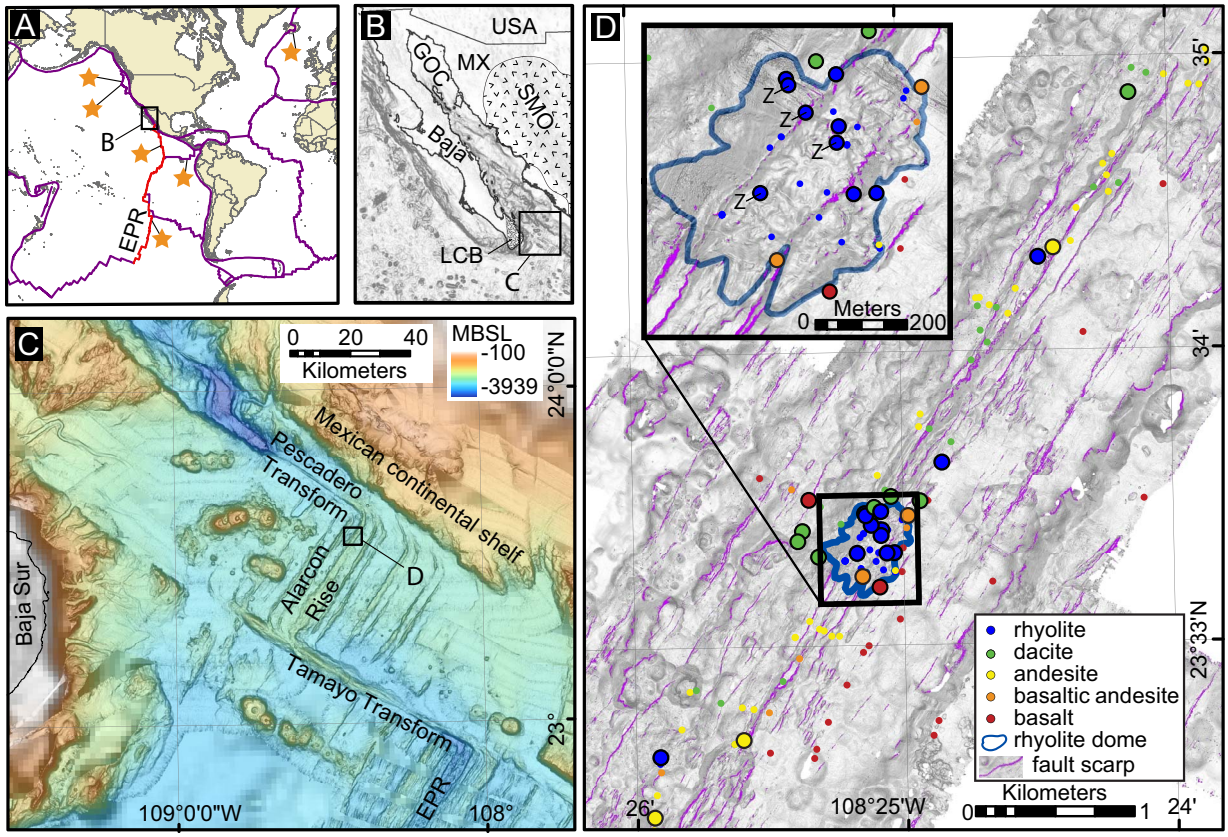

Fig. 1. Study site location maps. (A) Global map showing known locations of evolved MOR volcanic rocks (stars). All plate boundaries shown by purple lines except the EPR shown in red. Field area shown by box labeled B. (B) Regional map of the Gulf of California (GOC). Continental crust domains of the Sierra Madre Occidental (SMO) rhyolite province (Ferrari *et al.*, 2007) and granitic Los Cabos Block (LCB) are adjacent to field area shown by box labeled C. (C) Bathymetric map of Alarcon Rise MOR spreading ridge segment with study area shown by box labeled D at northern end of the spreading segment. Bathymetry of Alarcon Rise derived from ship-based multibeam data. (D) Locations of samples used in this study shown by larger symbols with black outlines. Close-up view of central rhyolite dome showing zircon samples denoted by 'Z'. Bathymetric data derived from autonomous underwater vehicle (AUV)-collected multibeam data and gridded to 1 m. Fault scarps with slopes >55° are highlighted by purple shading.

Sinton, 1981). Most existing models to explain the occurrence of evolved MOR lavas stem from tectono-magmatic processes that rely on episodic magma supply near spreading-ridge tips (Christie & Sinton, 1981), proximity to cold lithosphere (Perfit *et al.*, 1983), partial melting of hydrated oceanic crust in anomalously thick lithosphere (Nicholson *et al.*, 1991) or along deep-seated oceanic detachment faults (Koepke *et al.*, 2007; Jöns *et al.*, 2009), and/or some combination of these factors (Wanless *et al.*, 2010). Although MOR zircon is quite common in evolved plutonic rocks (e.g. Schwartz *et al.*, 2005; Grimes *et al.*, 2015), its presence is very rare in volcanic rocks (cf. Schmitt *et al.*, 2011) and has not been widely used to help understand the origin of unusually evolved MOR lavas. Rhyolite-hosted zircon and whole rock geochemistry and geochronology are used here to understand rhyolite petrogenesis on the Alarcon Rise MOR.

ALARCON RISE

Alarcon Rise is the northernmost spreading segment of the EPR and is located in the mouth of the Gulf of California ~8 km from the Mexican continental slope (Fig. 1C). Seafloor spreading along Alarcon Rise initiated by 2–3 Ma and evolved into a ~40-km long intermediate-rate spreading ridge (49 mm/a full rate) with normal MOR crustal thickness (5–7 km; Sutherland, 2006; Lizarralde *et al.*, 2007; DeMets *et al.*, 2010). The rise is volcanically active and bound by leaky transforms faults, the Pescadero to the north and the Tamayo to the south (Fig. 1C), both of which have young basaltic lava flows (Clague *et al.*, 2018).

Alarcon Rise, like most of the global MOR, is primarily made up of normal mid-ocean ridge basalt (N-MORB), but evolved compositions including basaltic andesite, andesite, dacite, and rhyolite make up a notable portion of the northern 25% of the rise (Castillo *et al.*, 2002; Clague *et al.*, 2018) and occur 10–5 km inboard from the Pescadero Transform (Fig. 1C). This northern part of the rise has a significantly higher number of exposed fault scarps than the rest of the rise (Fig. 2). The evolved lavas occur along a ridge-parallel lineament that is ~300 m in width and cut by abundant high-angle fault scarps (Fig. 1D). Three rhyolite domes 2–5 × 10^6 m^3 occur along the lineament in its southern, central, and northern areas. These domes were entirely effusive and are primarily composed of autoclastic breccia (Portner *et al.*, 2021). The largest and most silicic rhyolite dome occurs

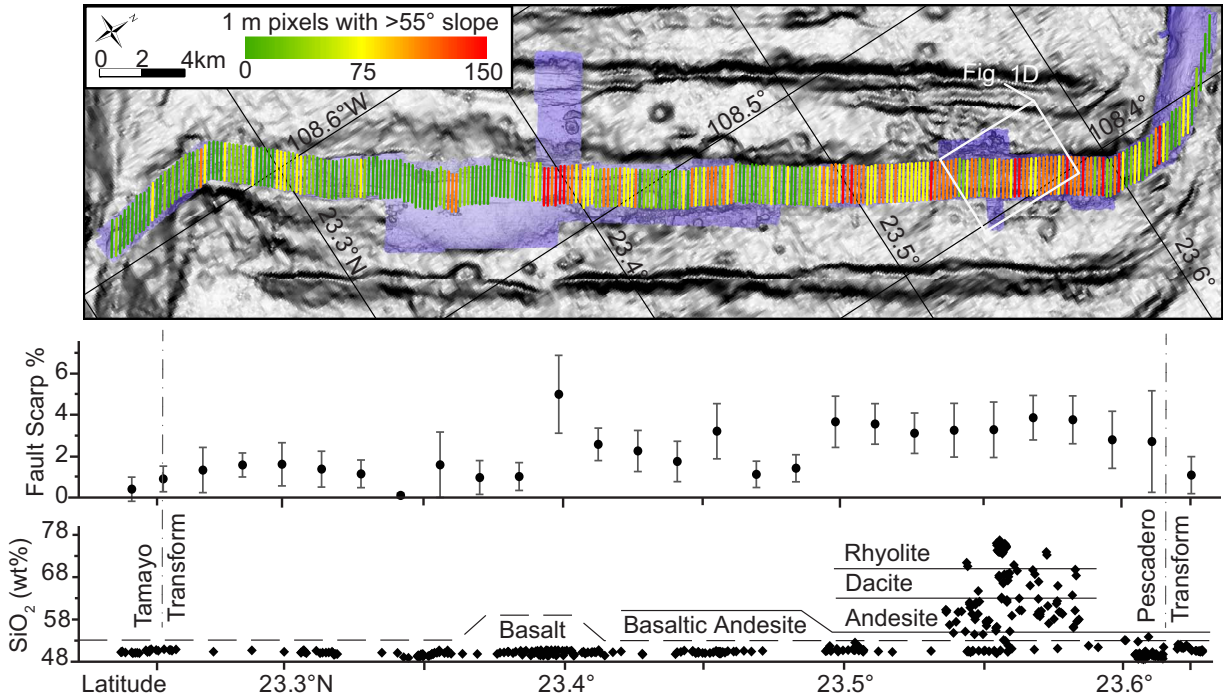

Fig. 2. Variation of lava composition and fault scarp proportion along Alarcon Rise. Map shows 1770 m long transect lines (green–yellow–red) that are color coded by length that is coincident with a fault scarp. Fault scarps are identified from purple 1-m resolution AUV bathymetry that has linear patterns of slopes >55° (Fig. 1D). Gray bathymetry is the same as that shown in Fig. 1C. Each data point in the plot of fault scarp % represents the average proportion of 10 transect lines where each data point is plotted at the center of the group of transects along the x-axis. Error bars are 1σ. Bottom plot shows electron microprobe-derived SiO_2 content from volcanic glass sampled from lavas along the ridge axis (data from Clague *et al.*, 2018).

at the lineament center and is the focus of this study (Fig. 1D inset).

A total of 362 lava samples from Alarcon Rise were collected by the remotely operated vehicles (ROVs) *Tiburon* and *Doc Ricketts* in 2003, 2012, and 2015 and greatly expand the prior collection of samples collected from six on-axis dredges from the 1990s (Castillo *et al.*, 2002). Although most lavas have incompatible element depletion typical of N-MORB, slightly enriched (E)-MORB were also collected from the Pescadero Transform and the central part of Alarcon Rise. Major element compositions across the full sample suite follow a tholeiitic trend (Fig. 3) that encompasses the full lithologic spectrum between basalt and rhyolite up to 77 wt% SiO_2 (Table 1). Compositional trends are partly consistent with Rhyolite-MELTS models of crystal fractionation under slightly reducing conditions (QFM-M1), but discrepancies in FeO and TiO_2 (outlined samples on Fig. 3) and enrichment in K_2O and Cl are thought to be associated with hybridization/mixing processes and incorporation of a seawater-based assimilant, respectively (Clague *et al.*, 2018).

Thirty-six samples were collected from the central rhyolite dome, whereas two samples were collected from both the southern and northern domes. Rhyolite samples are glassy and unaltered. Coarse to fine-grained mafic and intermediate xenoliths are common, display sharp contacts and are phyric (Fig. 4A). Rhyolites are moderately (10%–50%) vesicular and crystal rich (Portner *et al.*, 2021). Crystal contents range from ~15% to 30%, with

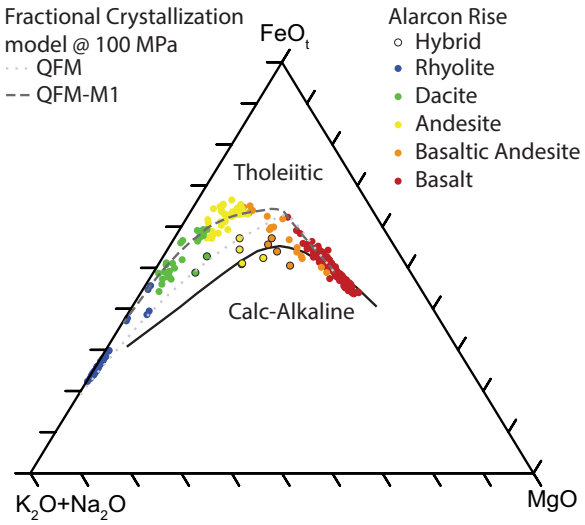

Fig. 3. Major element geochemistry (from Clague *et al.*, 2018) for lavas erupted on Alarcon Rise showing a tholeiitic trend. Hybrid samples (outlined) identified by Clague *et al.* (2018) as having relatively lower FeO and TiO_2 compared with the bulk of samples follow a similar, though lower FeOt, fractional crystallization trend. Both fractional crystallization trends modeled with Rhyolite-MELTS (Gualda *et al.*, 2012). Models start from the most magnesian sample (D398-R7 with 7.56 wt% MgO) adjacent to the central rhyolite dome. The parent basalt contains 0.25 wt% H_2O and 77 μg/g CO_2 (Portner *et al.*, 2021). Model runs at 100 and 35 MPa show little to no difference on this plot and are identical to the higher magnesian portions of trends starting from a more primitive sample with 8.6 wt% MgO (D395-R11) collected further south from the evolved volcanic suite (Clague *et al.*, 2018).

Table 1: Glass major element composition (wt%) from samples used in this study

Sample	Latitude	Longitude	Depth	SiO_2	TiO_2	Al_2O_3	FeO	MnO	MgO	CaO	Na_2O	K_2O	P_2O_5	Cl	S	Total
D392-R15	23.351472	−108.547998	2296	49.47	1.33	16.57	8.85	0.16	8.48	12.25	2.75	0.09	0.14	0.006	0.108	100.21
155-V36^	23.805833	−108.58683	2987	50.12	1.88	16.07	10.65	0.19	7.30	10.67	3.09	0.327	0.228	0.009	0.103	100.65
D746-R12	23.399844	−108.52809	2327	50.53	1.69	15.35	9.76	0.20	7.39	11.63	3.09	0.38	0.24	0.025	0.112	100.38
D398-R7	23.553275	−108.418212	2418	50.67	1.68	15.08	10.35	0.17	7.56	11.70	2.99	0.16	0.18	0.012	0.141	100.70
D740-R3	23.558271	−108.422505	2476	51.89	1.35	14.94	9.53	0.17	6.74	11.29	2.94	0.32	0.15	0.058	0.111	99.48
GOC12-RC11	23.612413	−108.38288	2353	52.83	1.71	14.60	10.66	0.21	5.16	9.62	3.59	0.40	0.28	0.049	0.127	99.22
D401-R33	23.557308	−108.416406	2401	52.97	2.04	13.95	12.11	0.22	4.91	8.74	3.84	0.45	0.28	0.076	0.142	99.73
D398-R6	23.553896	−108.419255	2372	55.36	1.97	14.08	12.27	0.23	3.70	7.34	3.99	0.68	0.51	0.164	0.108	100.41
D741-R5	23.540357	−108.432335	2430	59.77	1.50	14.82	8.46	0.12	2.75	5.93	4.26	1.17	0.19	0.254	0.059	99.28
D398-R16–2	23.544686	−108.42677	2384	60.85	1.38	13.38	10.29	0.21	1.34	4.46	5.21	1.14	0.48	0.288	0.073	99.12
D398-R16	23.572445	−108.407182	2349	61.23	1.20	12.60	11.98	0.31	0.79	4.56	4.82	1.03	0.36	0.217	0.095	99.20
D742-R15	23.544686	−108.42677	2384	61.69	1.37	13.46	10.59	0.20	1.37	4.44	4.52	1.09	0.46	0.288	0.068	99.54
D401-R29	23.557813	−108.418482	2341	62.65	1.10	13.40	10.45	0.20	0.96	4.14	5.08	1.09	0.31	0.263	0.061	99.72
D401-R2	23.555924	−108.423237	2475	63.24	1.04	13.21	10.05	0.19	0.89	3.86	5.06	1.20	0.30	0.312	0.052	99.39
D742-R24	23.581195	−108.40237	2411	63.77	1.27	14.02	8.46	0.15	1.39	4.11	4.82	1.35	0.33	0.271	0.046	99.99
D401-R1	23.5565	−108.42293	2482	66.87	0.73	13.40	7.26	0.15	0.54	2.85	5.16	1.59	0.17	0.413	0.023	99.17
D401-R34	23.558146	−108.415635	2393	67.25	0.65	13.03	7.25	0.17	0.32	2.68	5.66	1.56	0.13	0.323	0.030	99.05
D740-R17	23.55841	−108.417448	2355	68.14	0.64	12.67	7.29	0.18	0.39	2.53	4.92	1.67	0.13	0.375	0.029	98.97
D401-R3	23.555032	−108.421966	2418	68.43	0.64	13.05	6.78	0.15	0.49	2.43	5.16	1.75	0.12	0.489	0.029	99.52
D741-R8	23.543788	−108.431917	2472	70.60	0.68	13.13	4.91	0.09	0.48	1.98	5.02	2.04	0.14	0.375	0.010	99.45
D740-R21	23.560309	−108.414269	2411	70.92	0.46	12.57	5.68	0.14	0.13	1.88	5.07	1.84	0.06	0.380	0.012	99.13
D742-R13	23.571925	−108.408122	2353	73.98	0.29	11.39	4.25	0.07	0.07	1.18	4.94	2.22	0.03	0.525	—	98.94
D401-R20*	23.556208	−108.418077	2348	74.61	0.18	11.79	2.66	0.05	0.05	0.74	5.03	2.77	0.02	0.605	—	98.53
D401-R14	23.556532	−108.418037	2349	74.78	0.17	11.74	2.56	0.05	0.04	0.75	5.12	2.76	0.03	0.600	0.003	98.62
D401-R24*	23.556804	−108.418689	2325	74.87	0.21	11.96	2.77	0.06	0.04	0.77	5.21	2.70	0.01	0.613	0.003	99.21
D401-R28*	23.557343	−108.419029	2337	74.88	0.21	11.12	2.93	0.06	0.06	0.65	4.84	2.90	0.02	0.728	0.001	98.40
D401-R26	23.557468	−108.419075	2340	75.17	0.20	11.17	2.71	0.06	0.05	0.62	4.85	3.02	0.01	0.641	0.002	98.50
D401-R30	23.557561	−108.418088	2337	75.23	0.19	11.00	2.72	0.05	0.03	0.62	4.78	2.94	0.01	0.598	0.005	98.17
D401-R7*	23.555215	−108.419583	2347	75.50	0.16	11.23	2.24	0.03	0.02	0.55	4.84	2.94	0.01	0.540	0.006	98.06
D398-R3	23.555199	−108.417744	2380	75.59	0.20	12.05	2.95	0.07	0.09	0.85	4.84	2.52	0.03	0.591	—	98.36
D398-R2	23.55522	−108.417293	2400	76.77	0.21	11.06	2.99	0.06	0.07	0.65	4.12	2.81	0.04	0.638	—	99.42

All data were collected on electron microprobe (Clague *et al.*, 2018). *Samples used for zircon geochemistry and geochronology. ^Dredge sample collected from Pescadero transform in 1976 on cruise L176MX.

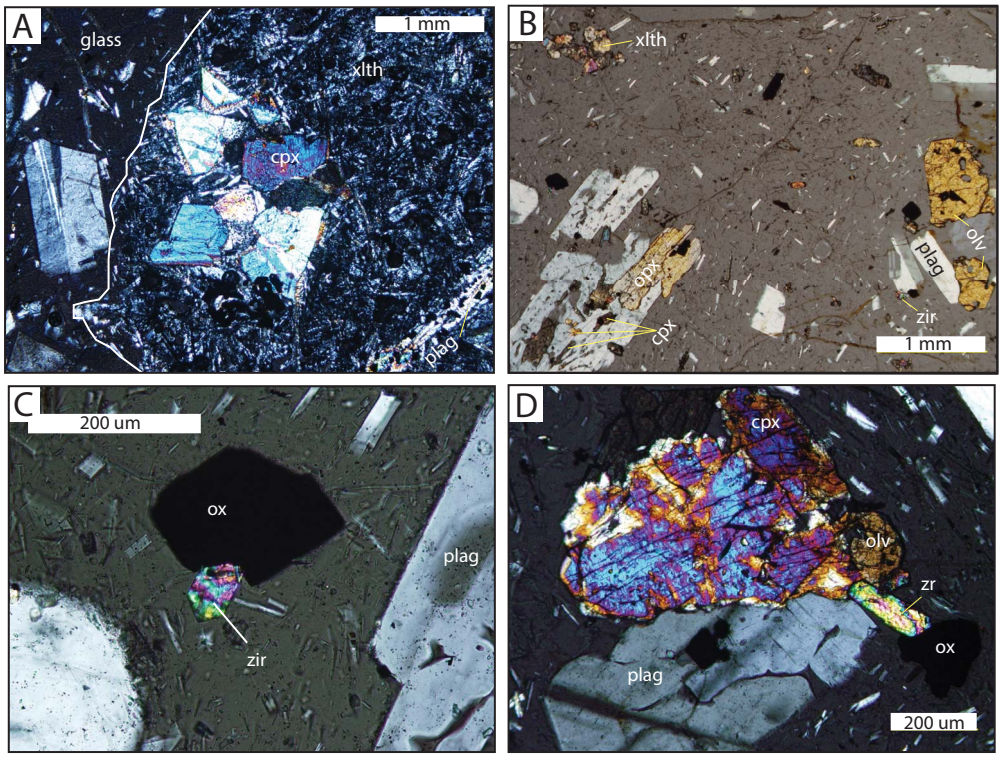

Fig. 4. Cross-polarized microphotographs of zircon-host rhyolite. Acronyms correspond to the minerals plagioclase (plag), clinopyroxene (cpx), othropyroxene (opx), olivine (olv), FeTi oxides—ilmenite or titanomagnetite (ox), and zircon (zir). (A) Crystalline phyric xenolith (xlth) with sharp contact against glassy rhyolite. (B) Representative rhyolite texture showing plagioclase microlites and glomerocrysts of plagioclase and mafic minerals. (C) Opaque FeTi oxide with attached euhedral zircon. (D) Glomerocrystic cluster containing primary phenocryst phases and accessory zircon.

some areas containing very high plagioclase microlite concentrations. Phenocrysts (250–1500 μm) of sodic plagioclase (oligoclase), fayalitic olivine, clinopyroxene, and orthopyroxene occur as isolated crystals and more commonly as glomerocrysts (Fig. 4B). Glomerocrysts also contain much finer-grained ilmenite and magnetite, which are primarily disseminated throughout the glass matrix. Trace amounts of apatite also occur within fayalite melt inclusions. Glomerocrysts and FeTi oxide minerals locally have trace quantities of attached zircon, which rarely occur alone (Fig. 4C and D). Zircon data presented here come from four rhyolite samples collected from the central rhyolite lava dome.

METHODS

Whole rock isotope analysis

Strontium, Nd, and Pb isotope ratios were analyzed using a 9-collector, Micromass Sector 54 thermal ionization mass spectrometer at the Scripps Institution of Oceanography, University of California San Diego. Total procedural blanks are 35 pg for Sr, 10 pg for Nd, and 60 pg for Pb. Strontium isotopic ratios were fractionation-corrected to $^{86}Sr/^{88}Sr = 0.1194$ and are reported relative to $^{87}Sr/^{86}Sr = 0.710254 + 0.000018$ ($n = 22$) for NBS 987 during the period of analysis. Neodymium isotopic ratios were measured in oxide form, fractionation-corrected to $^{146}NdO/^{144}NdO = 0.72225$ ($^{146}Nd/^{144}Nd = 0.7219$) and are reported relative to $^{143}Nd/^{144}Nd = 0.511856 \pm 0.000016$ ($n = 19$) for the La Jolla Nd Standard during the period of analysis. Lead isotopic ratios were analyzed using the double-spike method to correct for mass fractionation during analyses; separate measurements of spiked and unspiked samples were made on different aliquots from the same dissolution. The SBL-74 ^{207}Pb–^{204}Pb double-spike from the University of Southampton was used. During the analysis period, the method produced the following results for NBS981: $^{206}Pb/^{204}Pb = 16.9300 \pm 0.0020$, $^{207}Pb/^{204}Pb = 15.4896 \pm 0.0027$ and $^{208}Pb/^{204}Pb = 36.6999 \pm 0.0086$ ($n = 11$). 2σ precisions for individual runs are better than these.

Hafnium isotope ratios on whole rock samples were measured with a Neptune MC-ICP-MS at the Keck Isotope Laboratory at the University of California Santa Cruz. Hafnium was separated from digested samples with Ln-spec resin following Munker *et al.* (2001). Hf isotopes were exponentially normalized internally to $^{179}Hf/^{177}Hf = 0.7325$. Sample data were normalized to JMC 475 $^{176}Hf/^{177}Hf = 0.282160$ (Blichert-Toft & White, 2001), which was measured at the beginning of each analytical session and after every three unknowns. Seven analyses of JMC yielded an average of $^{176}Hf/^{177}Hf = 0.282145 \pm 10$ (2σ). Whole rock hafnium isotope data are reported as $\varepsilon Hf_{wholerock}$, which is calculated by $[(^{176}Hf/^{177}Hf_{sample}/^{176}Hf/^{177}Hf_{CHUR})\text{-}1] \times 10\,000$ where the hafnium isotope value of the chondritic uniform reservoir ($^{176}Hf/^{177}Hf_{CHUR}$) is 0.282785 (Bouvier *et al.*, 2008).

Hydrogen and oxygen isotopes and total water concentrations were measured in duplicate or triplicate on 1–2-mg glass fragments by laser fluorination ($\delta^{18}O$) and ~30 mg of 50–250-μm glass chips by thermal conversion/elemental analyzer (TC/EA; δD and H_2O_t) coupled to a large radius MAT253 10-kV gas source isotope ratio mass spectrometer at the Stable Isotope Lab at the University of Oregon (Bindeman *et al.*, 2012*b*; Martin *et al.*, 2017). Oxygen isotope notation, $\delta^{18}O$, is defined as $[(^{18}O/^{16}O_{sample})/(^{18}O/^{16}O_{VSMOW})\text{-}1] \times 1000$, where the Vienna Standard Mean Ocean Water (VSMOW) standard $^{18}O/^{16}O_{VSMOW} = 0.0020052$. Hydrogen isotope notation, δD, is defined as $[(D/H_{sample})/(D/H_{VSMOW})\text{-}1] \times 1000$, where $D/H_{VSMOW} = 0.00015576$. Measurement uncertainty (all reported as 2σ) for δD in ‰, parts/thousand, and H_2O_t in wt% is based on concurrently run NBS30 (-66.67 ± 1.45‰; 3.57 ± 0.17 wt%), RUH (-97.03 ± 2.51‰; 4.60 ± 0.26 wt%), and BUD (-163.10 ± 2.04‰; 2.32 ± 0.24 wt%) standards.

Zircon sample preparation

Four glassy rhyolite lava samples yielded ~110 zircon grains per kilogram of rock. Samples were pulverized by high-voltage electrodynamic disaggregation using SelFrag©, which fragmented the samples along grain boundaries preserving complete crystal shapes. Heavy minerals, including zircon, were then concentrated using traditional heavy liquid and magnetic techniques. Extracted zircons were prepared in epoxy mounts and polished. Cathodoluminescence (CL) images were used to identify core and rim associations and guide laser ablation spot analyses.

Zircon U-series ion microprobe (SHRIMP-RG) analysis

Zircons from the four rhyolites were measured for U and Th isotopes at the sensitive high resolution ion microprobe-reverse geometry (SHRIMP-RG) facility at Stanford University. Twenty unknown spot analyses were bracketed by zircon 91500 (Wiedenbeck *et al.*, 2004). Beam sizes were 25×35 μm and sputtered 3–5 μm deep into the sample. Median zircon U and Th concentrations were 143 and 93 μg/g, respectively. Ten analyses of zircon from the Early Bishop Tuff (EBT) were measured at the beginning of each analytical session, and the average $^{238}U/^{232}Th$ was used to correct unknowns. Repeat analyses of EBT on 2 days gave averages of $^{238}U/^{232}Th = 0.9612 \pm 0.0071$ (2σ, $n = 14$) and 0.9681 ± 0.0083 ($n = 9$), respectively. Model ages were calculated using decay constants $\lambda_{230} = 9.1577 \times 10^{-6}$ a^{-1}, $\lambda_{232} = 4.9475 \times 10^{-11}$ a^{-1}, and $\lambda_{238} = 1.55125 \times 10^{-10}$ a^{-1} (Supplementary Table S1).

Zircon trace element LA-ICPMS

Zircon trace elements were analyzed by LA-ICPMS in the geo-analytical unit of Macquarie University, Sydney, Australia, which operates a New Wave 213 nm Nd:YAG laser system linked to an Agilent 7500 s ICP-MS (Jackson *et al.*, 2004). Analyses used a beam diameter of 30–40 μm, a 5-Hz repetition rate, and an output energy of ~0.9 mJ per pulse. Synthetic glass (NIST-610 and BCR) and zircon (GJ-1) standards were used to evaluate accuracy and precision (Supplementary Table S2). Analysis runs were collected in batches of 15 measurements of unknowns between measurements of three to five standards over 3 days of data collection.

Non-zircon phases (e.g. apatite, xenotime, FeTi oxides) exposed at the surfaces of zircon grains were avoided during laser ablation. Some of these inclusions were ablated as the laser penetrated into a grain's subsurface and were characterized by anomalously high contents of P, heavy rare earth element (HREE), Fe, and/or Ti. If present, data from subsurface inclusions were filtered from sample analyses so that only zircon data were evaluated. In these cases, the shortened analysis times were less precise than 'clean' analyses, but both groups span the same elemental concentration range.

Zircon Hf isotope LA-MC-ICPMS

Following trace element analysis, zircons were analyzed for $^{176}Hf/^{177}Hf$ using LA-MC-ICPMS at Macquarie University. A New Wave Research 213 nm Nd:YAG laser, connected to a Nu Plasma multi-collector ICP-MS was used with a beam diameter of 55–45 μm, 5-Hz repetition rate, and 1.3–0.6-mJ output energy/pulse. Nu plasma time-resolved analysis software was used to select stable portions of the measurement and calculate standard error. Smaller signal selection is reflected by larger internal analytical error. The average percent signal selection used for reported $^{176}Hf/^{177}Hf$ data is 78% with no discernable difference between the average or range of data with different signal selection percentages. For some measurements, the latter portions of the signal were excessively noisy due to accidental ablation of inclusions or from ablation through small zircon grains and into the epoxy mount. If stable portions of the analysis accounted for <30% of the full analysis, it was expunged from the dataset ($n = 6/121$). Zircon hafnium isotope data are reported as εHf_{zircon}, which is calculated using the same equation as $\varepsilon Hf_{wholerock}$.

Interference of ^{176}Lu and ^{176}Yb on ^{176}Hf was corrected by measuring the interference-free ^{175}Lu and ^{172}Yb isotopes and using $^{176}Lu/^{175}Lu$ (0.02669 after De Bievre & Taylor, 1993) and $^{176}Yb/^{172}Yb$ (0.58669 after Griffin *et al.*, 2002) to calculate $^{176}Lu/^{177}Hf$ and $^{176}Yb/^{177}Hf$. Repeated calibration of standards has shown that $^{176}Hf/^{177}Hf$ is accurate when $^{176}Yb/^{177}Hf \leq 0.26$ but becomes increasingly less precise when $^{176}Yb/^{177}Hf > 0.20$ (Griffin *et al.*, 2000, 2002). Analyses with $^{176}Yb/^{177}Hf$ values 0.20–0.26 and >0.26 are indicated on all plots ($n = 30/115$ analyses).

Measured isotopic ratios of the Mudtank and Temora zircon standards (Woodhead & Hergt, 2005) were used to assess accuracy and precision of zircon analyses. Analytical runs were collected in batches of three to six measurements of unknowns between measurements of two to three standards over 3 days of data

collection. The mean value measured for Mudtank zircon during the 3 days ($n = 40$) of this study was $^{176}Hf/^{177}Hf = 0.282539 \pm 42$ (2σ), which is well within uncertainty of the accepted value 0.282523 ± 59 (2σ; Gain *et al.*, 2019). Slight positive and negative trends between $^{176}Hf/^{177}Hf$ vs $^{178}Hf/^{177}Hf$ and $^{180}Hf/^{177}Hf$, respectively, exist for the Mudtank standard but still fall within 2σ error (Supplementary Table S3). The Temora zircon standard has a much higher Yb content and is therefore better for evaluating the Yb-interference correction on unknown Alarcon Rise grains. Measurements at the start and end of each day of analysis yield an average $^{176}Yb/^{177}Hf$ ($n = 7$) of 0.0434 ± 41 (2σ) and $^{176}Hf/^{177}Hf$ of 0.282683 ± 54, which are within analytical error of accepted values 0.032 ± 15 and 0.282680 ± 31, respectively (Wu *et al.*, 2006). Importantly, no trends between $^{176}Yb/^{177}Hf$ and $^{176}Hf/^{177}Hf$ in either the Mudtank or Temora standards were observed indicating that the Yb-correction factor was acceptable.

Zircon $\delta^{18}O$ secondary ion microprobe (SIMS) analysis

Zircon oxygen isotopes were measured with the Cameca IMS-1280 at the University of Wisconsin, Madison WiscSIMS facility. Zircon grains from two rhyolite samples were carefully polished to ensure a smooth, flat, low-relief surface (Kita *et al.*, 2009). Analyzed spot sizes were ~10 μm. Zircon standard KIM-5 was measured five times before and after every 10 samples. The average $^{18}O/^{16}O$ of KIM-5 over the course of the analytical run was 4.75 ± 0.42‰ (Supplementary Table S4). Grain measurements were then corrected to KIM-5 $\delta^{18}O$ of 5.09‰ (Valley, 2003).

RESULTS

Whole rock isotopes and water concentrations

Whole-rock Sr-Nd-Pb isotope analyses of representative Alarcon lavas compare well with EPR lavas. Rhyolites exhibit subtly higher $^{87}Sr/^{86}Sr$ than most other compositions (Table 2) but still cluster near depleted MORB mantle (DMM) in Nd-Sr isotope space (Fig. 5A). One E-MORB and one dacite both have affinities closer to an enriched DMM (EDMM) source in all Sr-Nd-Pb plots. Lead isotopes show no correlation with degree of differentiation and form a trend from DMM to a slightly enriched source where $^{206}Pb/^{204}Pb$ ranges from 18.4 to 18.7 (Fig. 5B and C). Hafnium isotopes on five rhyolite samples yield an average $\varepsilon Hf_{wholerock}$ of 13.06 ± 0.14 (2σ), which does not differ from the basalt to dacite average of 13.01 ± 0.44 (Fig. 6A).

Rhyolites ($n = 4$) have a narrow range in $\delta^{18}O_{wholerock}$ with an average of 6.23 ± 0.16‰ and represent the evolved end of a near-linear trend from mafic to intermediate compositions (Fig. 6B). The mafic end-member is within analytical error of the accepted N-MORB value of 5.7 ± 0.2‰ (Table 2). Compared with modeled fractionation trends, Alarcon Rise lavas plot closest to the 'normal' (mantle-derived) high magnesium $\delta^{18}O$ array of

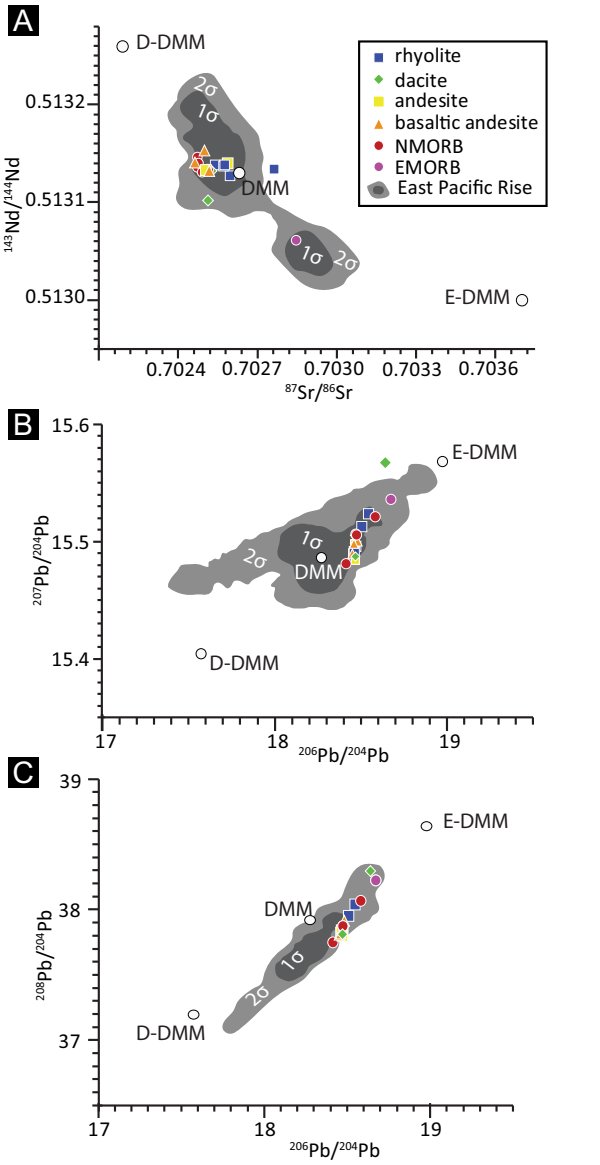

Fig. 5. Whole rock Sr-Nd (A) and Pb–Pb (B–C) isotope data for all lava compositions from Alarcon Rise. Depleted (D-) and enriched (E-) end-members of the DMM reservoir are from Workman & Hart (2005). Dark (1σ) and light (2σ) gray fields represent contoured point density plots of EPR spreading center Sr-Nd ($n = 307$) and Pb–Pb ($n = 252$) isotope data from PetDB. Point density plots created using ArcGIS spatial analyst software.

Bindeman (2008) and slightly lower than other models for MORB and the more hydrous Bushveld layered intrusive complex (Bucholz *et al.*, 2017). Lava compositions all have much lower $\delta^{18}O$ than model trends used for Ocean Island and hotspot-affected regions (Muehlenbachs & Byerly, 1982; Sheppard & Harris, 1985).

Hydrogen isotopes (δD) generally range between −60‰ to −65‰ with a smaller subpopulation of −75‰ to −80‰ (Fig. 6C). This range is larger than the analytical uncertainty of 2.46‰ on each measurement. The larger population is within error of average Pacific N-MORB (-60 ± 5‰) while the smaller population extends to a more enriched variant sampled along the EPR around 17–15°N (Clog *et al.*, 2013; Dixon *et al.*, 2017). Alarcon δD does

Table 2: Whole rock isotope and water concentrations.

Sample	SiO_2[#] (wt%)	$^{87}Sr/^{86}Sr$		$^{143}Nd/^{144}Nd$		$^{206}Pb/^{204}Pb$		$^{207}Pb/^{204}Pb$		$^{208}Pb/^{204}Pb$		$^{176}Hf/^{177}Hf$		εHf		$\delta^{18}O$ (‰) ±0.16	δD (‰) ±2.46	H_2O (wt%) ±0.12
D392-R15	49.47	—	—	—	—	—	—	—	—	—	—	—	—	—	—	5.73	−77.97	0.19
155-V36	50.12	0.702846	±6	0.513061	±8	18.678	±3	15.536	±3	38.217	±8	—	—	—	—	—	—	—
D746-R12	50.53	—	—	—	—	—	—	—	—	—	—	0.283128	±19	12.48	±0.69	—	—	—
D398-R7	50.67	—	—	—	—	—	—	—	—	—	—	0.283137	±23	13.09	±0.80	5.61	−80.70	0.19
D740-R3	51.89	—	—	—	—	—	—	—	—	—	—	0.283149	±22	13.23	±0.78	—	—	—
GOC12-RC11	52.83	0.702510	±17	0.513133	±14	18.477	±3	15.506	±1	37.870	±3	—	—	—	—	5.77	−65.56	0.60
D401-R33	52.97	0.702519	±15	0.513132	±14	18.452	±3	15.490	±2	37.809	±5	—	—	—	—	5.79	−61.14	0.70
D398-R6	55.36	—	—	—	—	—	—	—	—	—	—	—	—	—	—	5.78	−60.53	0.93
D741-R5	59.77	—	—	—	—	—	—	—	—	—	—	0.283137	±13	13.10	±0.46	—	—	—
D398-R16–2	60.85	—	—	—	—	—	—	—	—	—	—	0.283146	±16	13.11	±0.57	—	—	—
D398-R16	61.69	—	—	—	—	—	—	—	—	—	—	0.283144	±17	13.05	±0.59	—	—	—
D742-R15	61.23	—	—	—	—	—	—	—	—	—	—	0.283136	±19	13.06	±0.68	—	—	—
D401-R29	62.65	0.702588	±18	0.513140	±12	18.467	±4	15.498	±1	37.843	±5	—	—	—	—	5.92	−62.23	1.73
D401-R2	63.24	0.702505	±12	0.513133	±6	18.468	±3	15.484	±1	37.801	±3	—	—	—	—	6.08	−64.42	1.95
D742-R24	63.77	—	—	—	—	—	—	—	—	—	—	0.283138	±18	13.12	±0.63	—	—	—
D401-R1	66.87	—	—	—	—	—	—	—	—	—	—	—	—	—	—	5.95	−59.76	1.98
D401-R34	67.25	0.702512	±14	0.513102	±20	18.641	±3	15.567	±1	38.293	±1	—	—	—	—	—	—	—
D740-R17	68.14	—	—	—	—	—	—	—	—	—	—	0.283139	±36	12.90	±1.27	—	—	—
D401-R3	68.43	0.702527	±12	0.513132	±6	18.47a1	±3	15.487	±1	37.809	±3	—	—	—	—	6.07	−64.21	1.63
D741-R8	70.60	—	—	—	—	—	—	—	—	—	—	0.283145	±16	13.10	±0.57	—	—	—
D740-R21	70.92	—	—	—	—	–	—	—	—	—	—	0.283133	±18	12.96	±0.65	—	—	—
D742-R13	73.98	—	—	—	—	—	—	—	—	—	—	0.283138	±20	13.14	±0.70	—	—	—
D401-R20*	74.61	0.702572	±17	0.513137	±22	18.463	±3	15.491	±3	37.823	±5	0.283138	±16	13.14	±0.56	—	—	—
D401-R14	74.78	—	—	—	—	—	—	—	—	—	—	—	—	—	—	6.14	−59.53	2.04
D401-R24*	74.87	0.702576	±20	0.513138	±18	18.508	±2	15.513	±1	37.949	±2	0.283135	±13	13.04	±0.45	—	—	—
D401-R28*	74.88	0.702763	±20	0.513134	±14	18.545	±4	15.524	±3	38.039	±5	0.283143	±19	13.03	±0.66	—	—	—
D401-R26	75.17	—	—	—	—	—	—	—	—	—	—	—	—	—	—	6.19	−63.55	1.65
D401-R30	75.23	—	—	—	—	—	—	—	—	—	—	0.283134	±15	13.00	±0.54	—	—	—
D401-R7*	75.50	0.702597	±14	0.513127	±18	18.461	±4	15.489	±3	37.818	±6	—	—	—	—	—	—	—
D398-R3	75.59	0.702541	±14	0.513138	±16	18.473	±2	15.496	±1	37.836	±3	—	—	—	—	6.30	−62.11	2.50
D398-R2	76.77	—	—	—	—	—	—	—	—	—	—	—	—	—	—	6.29	−76.04	1.96

All analytical error reported to 2σ. *Samples used for zircon geochemistry and geochronology. [#]Denotes glass composition form Table 1.

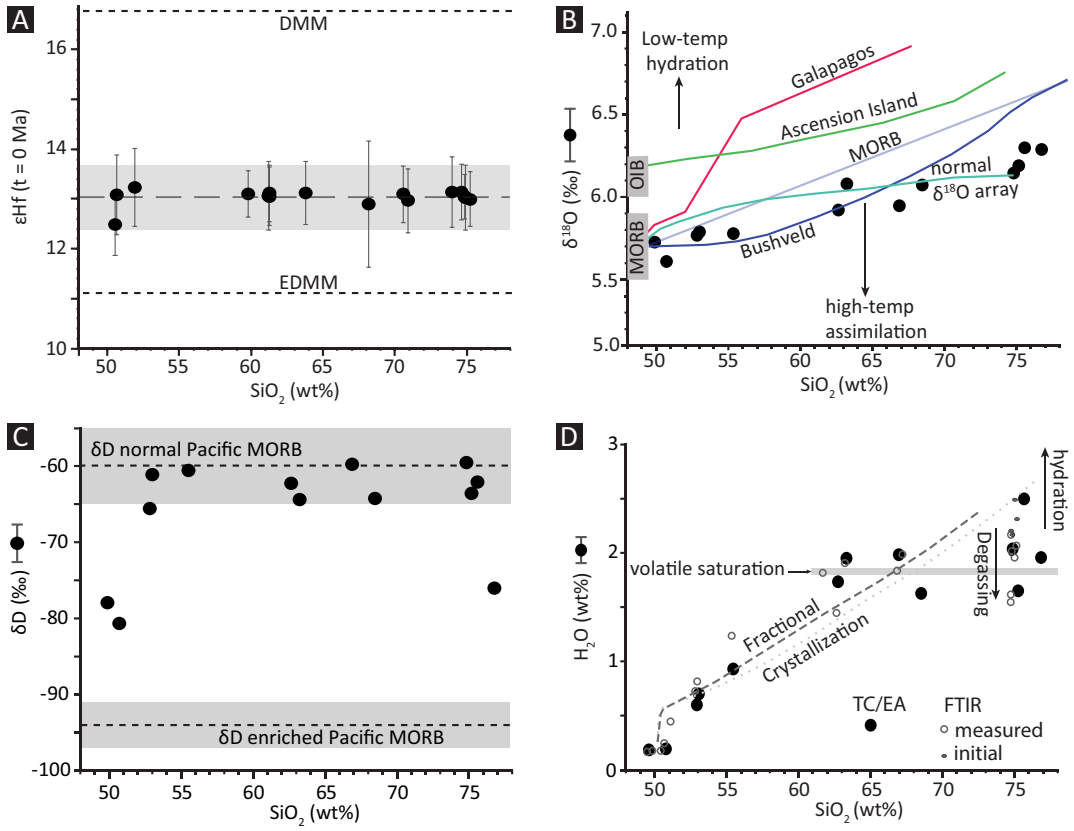

Fig. 6. Whole rock Hf, O, and H isotope data. SiO_2 compositions are from glass electron microprobe data (Clague *et al.*, 2018). (A) Epsilon Hafnium (εHf) values for depleted (D-) and enriched (E-) end-members of the DMM reservoir (short-dashed lines) are from Workman & Hart (2005). Average of all Alarcon lavas (long-dashed line) $\pm 2\sigma$ are shown by gray field. Individual sample analytical error bars are $\pm 2\sigma$. (B) Whole rock $\delta^{18}O$ data yield an average 2σ analytical precision of 0.16‰ (thick bar on y-axis). Fractionation trends (colored lines) from a starting MORB composition of 5.7‰ are from Bindeman (2008; high magnesium normal $\delta^{18}O$ array), Bucholz *et al.* (2017; MORB and Bushveld igneous complex), Sheppard and Harris (1985; Ascension Island alkaline suite), and Muehlenbachs and Byerly (1982; hot-spot influenced Galapagos Spreading Center). (C) Whole rock δD data yield an average 2σ analytical precision of 2.5‰ (bar on y-axis). Normal to enriched Pacific MORB δD values (dashed lines with 2σ gray area) from Clog *et al.* (2013) and Dixon *et al.* (2017). (D) Whole rock H_2O collected by TC/EA. Average 2σ analytical uncertainty is 0.12 wt%. Dissolved water contents measured by transmission FTIR are from Portner *et al.* (2021). Initial H_2O contents for non-pumiceous (<30% vesicles) rhyolites were calculated by recombining the FTIR-generated dissolved wt% H_2O with the exsolved wt% gas phase (assuming negligible CO_2). Exsolved wt% H_2O was calculated using the ideal gas law and vesicle volumes (Portner *et al.*, 2021) for the pressure at the depth of eruption (~23 MPa) and magma temperature of 766°C (see Ti-in-zircon thermometry below). These conditions were also used to calculate the solubility limit of H_2O for intermediate to felsic compositions (gray bar; Newman & Lowenstern, 2002). Fractional crystallization models are described in Fig. 3.

not show any consistent variation with composition and indicates a depleted to slightly enriched MORB mantle source.

Total water contents measured with TC/EA in this study agree well with published primary magmatic H_2O_{total} data collected by FTIR across all compositions (Fig. 6D). Overall increasing H_2O with SiO_2 follows a normal fractional crystallization trend up until ~62 wt% SiO_2, where water saturation is reached. At higher SiO_2 contents intermediate through felsic compositions mostly vary between 1.6 to 2.0 wt% H_2O, which is similar, to slightly above, expected concentrations for the solubility limit at the depth/pressure (~23 MPa) of eruption (assuming <10 μg/g CO_2). In this context, rhyolite H_2O concentrations lower than expected from fractional crystallization (2.4–2.7 wt% H_2O) are due to degassing, which is preserved by vesicularities of 10%~50% (Portner *et al.*, 2021). Aside from rare pumiceous samples (>30% vesicles), initial dissolved H_2O contents in rhyolites prior to bubble exsolution fall closer to expected concentrations (Fig. 6D). One rhyolite sample with up to 2.5 wt% H_2O (measured with TC/EA) may indicate secondary seawater hydration. This is confirmed by relatively high H_2O_m:OH (>1.2) in other hydrous rhyolites measured with FTIR (>>2.5 wt% H_2O_{total} [= H_2O_m + OH] not shown in Fig. 6D) due to faster diffusion rates of molecular water (H_2O_m) compared with hydroxyl (OH^-) species at low temperature (Portner *et al.*, 2021). However, a δD value of −62.11‰ for the aforementioned rhyolite sample (Table 2) does not deviate from other samples having Pacific MORB-affinities, implying that its 2.5 wt% H_2O may not be from secondary hydration (cf. Martin *et al.*, 2017) but instead reflects an undegassed primary magmatic volatile component.

Zircon textures and geochronology

Zircons form euhedral crystals that range from 250 × 30 to 80 × 50 μm. Some grains show little to no internal zonation (Fig. 7A), but most contain well-defined sector and oscillatory zoning (Fig. 7B and C) that is defined

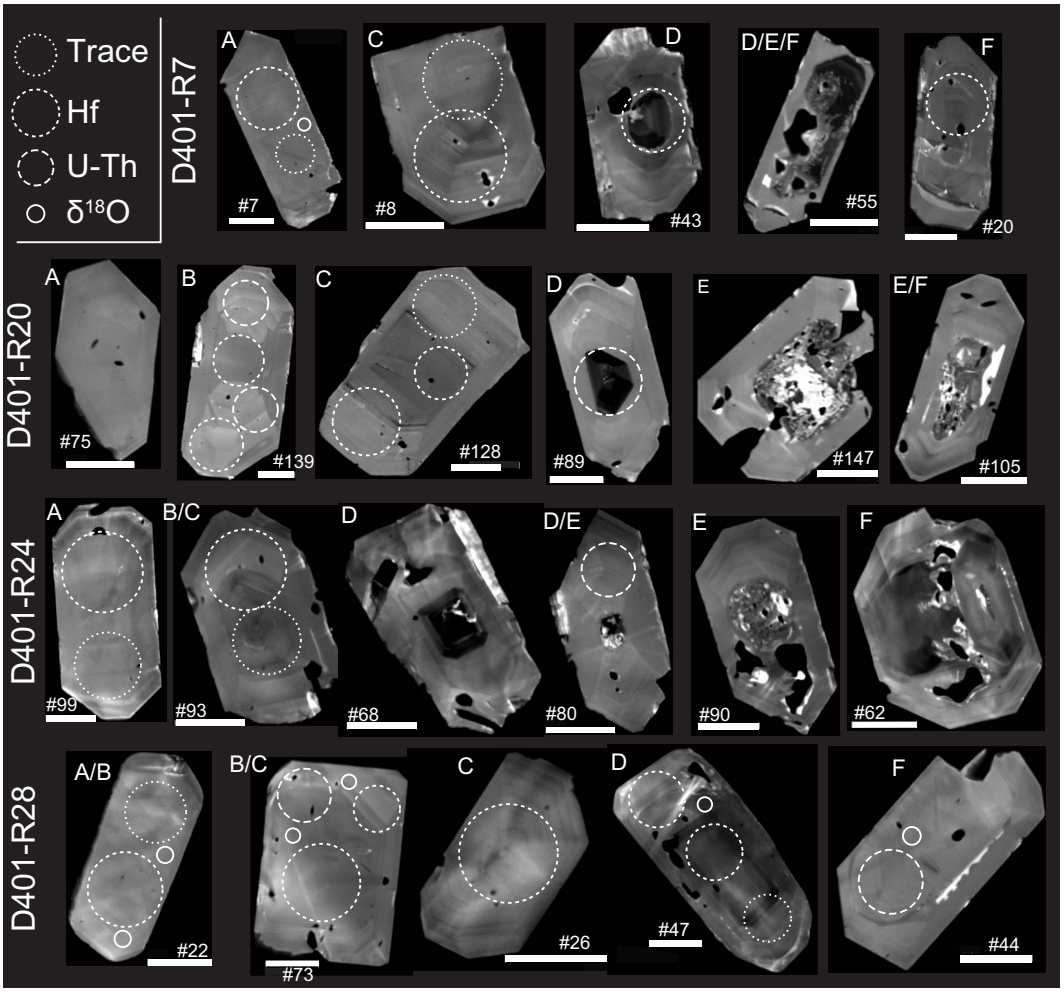

Fig. 7. CL images of representative Alarcon Rise zircons from four samples used for geochemistry and geochronology in this study. Grains exhibit faint to no internal zonation (A), sector zoning (B), oscillatory zoning (C), dark euhedral cores (D), porous or inclusion filled cores with numerous bright domains (E), and anhedral cores with marked zoning discontinuities along contacts with outer rim domains (F). Laser ablation pits (short-dashed circles) for hafnium (Hf) and trace elements (t) range from ~50 to 35 μm, respectively. Ion probe pits (long-dashed and solid circles) from U-Th analyses and $\delta^{18}O$ are 30 and ~10 μm, respectively. All scale bars are 40 μm.

by relatively bright and dark domains in CL imaging. Of 450 zircons imaged from four samples, 25% have darker CL fluorescence in their cores compared with rims (Fig. 7D) and 7% have porous or inclusion-rich cores with very bright CL (Fig. 7E). Most core-to-rim transitions are continuous with oscillatory zoning and no marked contact, but rare more anhedral to subhedral cores also occur with marked discontinuities in zonation patterns where they are in contact with more euhedral outer rims (Fig. 7F). The core-to-rim contact surfaces in discontinuously zoned grains locally exhibit <5 μm thick reaction domains that have unusually bright CL fluorescence. In some cases, multiple grain cores appear to be fused together (e.g. grain #62 in Fig. 7F). Grains with porous and inclusion-rich domains were avoided during trace element and isotope analysis.

SHRIMP U-Th zircon model ages from four samples yielded a pooled ($n = 71$) weighted mean age of 23.4 ± 4.5 (2σ) ka and a small population ($n = 5$) at 45 ± 9 ka (Fig. 8). Host glass (^{238}U)/(^{232}Th) and (^{230}Th/^{232}Th) from ICP-MS analyses average 0.95 ± 0.050. No discernable age difference was determined between core and rim spot analyses. The primary age population is consistent with a minimum eruption age of 11.7 ka derived from ^{14}C dating of foraminifera in sediment horizons that contain rhyolitic ash collected in push cores near the rhyolite dome (Clague *et al.*, 2018; Portner *et al.*, 2021).

Zircon trace element geochemistry

Rare earth element (REE) patterns for Alarcon zircon ($n = 111$) are mostly indistinguishable from other MOR magmatic zircon datasets, with depleted light (L)REE and negative Eu and positive Ce anomalies (Fig. 9A). Alarcon LREE patterns are slightly flatter compared with the global MOR crust survey (Grimes *et al.*, 2009) with a few grains (n~7) showing relatively small Ce anomalies, very low Sm_N/La_N and high La concentrations (Fig. 9B). Although the latter is common in porous zircon formed by dissolution-precipitation processes associated with hydrothermal fluids (Hoskin, 2005; Grimes *et al.*, 2009), clean oscillatory and sector zoning

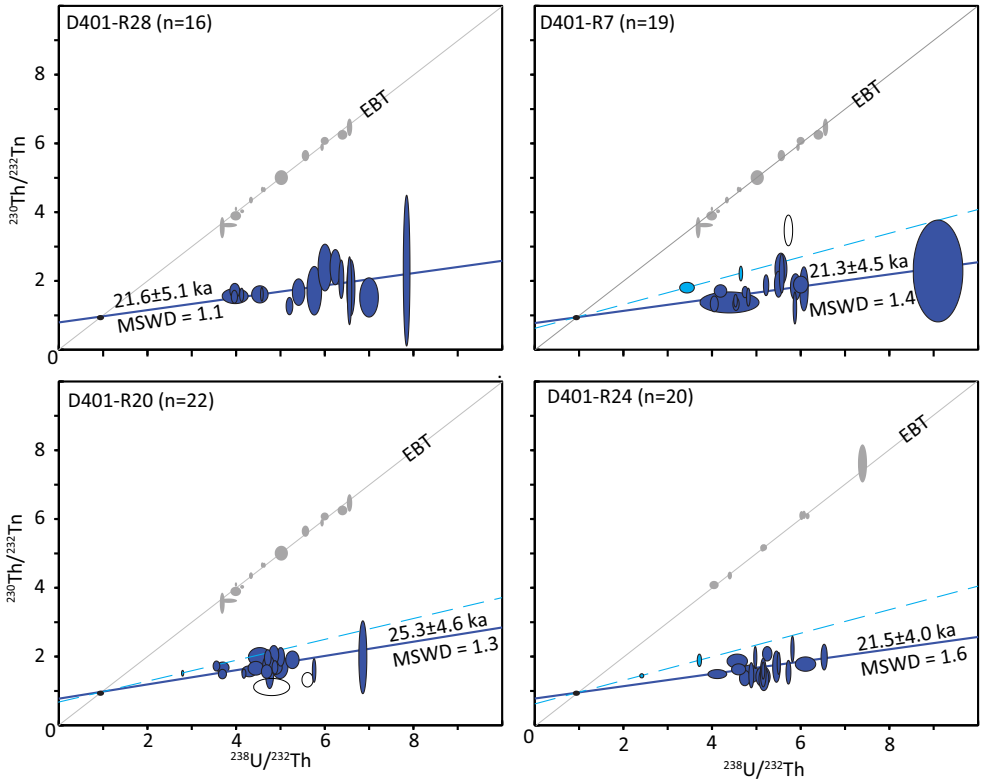

Fig. 8. U-Th activity diagram for zircons from four Alarcon Rise rhyolite samples. U-Th isochron model ages (dark blue grains) forced to intersect mean host glass U/Th value of 0.95 ± 0.05 (black ellipse). All error ellipses are 1σ. Dashed line through light blue grains yields combined age of 45.2 ± 8.9 ka (MSWD = 0.083). Three empty ellipses are grains expunged from isochron analysis. Light gray grains and corresponding isochron represent analyses from EBT on first (D401-R28, R7, and R20) and second (D401-R24) days of analyses. Plots made using IsoplotR (Vermeesch, 2018).

patterns in the Alarcon grains with low Sm_N/La_N are more indicative of a magmatic origin (Fig. 7B and C). Smaller Eu anomalies (Eu/Eu∗) and larger Ce anomalies (Ce/Ce∗) tend to correlate with higher total (Σ) REE concentrations (Fig. 9C and D). Grain cores generally have higher ΣREE but smaller Ce/Ce∗ and Eu/Eu∗ compared with rims.

Compared with zircon formed in continental settings, Alarcon Rise grains have low overall Hf (<1.1 wt%) and much higher Yb concentrations (>1000 μg/g; Fig. 10). The latter is typical for most MOR zircon grains, which also contain much higher Gd concentrations. Harker plots of Yb vs more incompatible trace elements exhibit overall positive trends with Alarcon Rise zircons having a closer affinity to 'normal' MOR zircon than grains from the hotspot-influenced MOR of Iceland or oceanic arcs (Fig. 10). Alarcon Rise zircon rims are slightly more depleted in Yb than cores and tend to be more enriched in Nb, Ce, Th, and U. Moreover, enrichment in all of these elements, as well as Gd, is also shared by MOR zircons interpreted to have formed from fractional crystallization processes rather than by partial melting of hydrous oceanic crust (Pietranik *et al.*, 2017).

Strong positive correlation between U and Yb in zircon reflects their similar compatibility (Fig. 10). However, since U is slightly less compatible than Yb (Nardi *et al.*, 2013), the U/Yb ratio increases during crustal evolution and is effective in discriminating oceanic vs continental/arc provenance (Grimes *et al.*, 2007). Plotting U vs Yb and U/Yb against other trace elements and ratios effectively shows a lower boundary of continental zircon in a survey of >5000 grains (Grimes *et al.*, 2015). Such plots indicate that Alarcon Rise zircon show a strong MOR affinity with little to no continental signature (Figs 10 and 11A–C).

Although data plot along the mantle array (Fig. 11C), analyses from zircon rims tend to yield consistently higher U/Yb ratios compared with core analyses (Fig. 11D). This trend is caused by lower Yb concentrations at a given U content in grain rims (Fig. 10). Grain rims also have higher Nb/Yb and slightly lower Gd/Yb, which corresponds with expected trends produced by zircon and apatite crystallization in the host melt (Fig. 11C and D; Grimes *et al.*, 2015). Increasing U/Yb during zircon growth is also corroborated by an overall positive trend with Hf (Fig. 11B), which increasingly substitutes for Zr during magma evolution and cooling (Grimes *et al.*, 2009).

Higher Hf concentrations also correspond with lower Ti-contents, a proxy for cooler temperatures (Fig. 12A). Titanium concentrations range from 5 to 24 μg/g, which corresponds to Ti-in-zircon crystallization temperatures between 700°C and 850°C (Fig. 12B). An average Ti-in-zircon temperature of 766 ± 53°C is within error of FeTi oxide temperatures of 811 ± 54°C (Portner *et al.*, 2021). The absence of trends in Ti and Hf between cores and rims from different grains indicates that they all did not

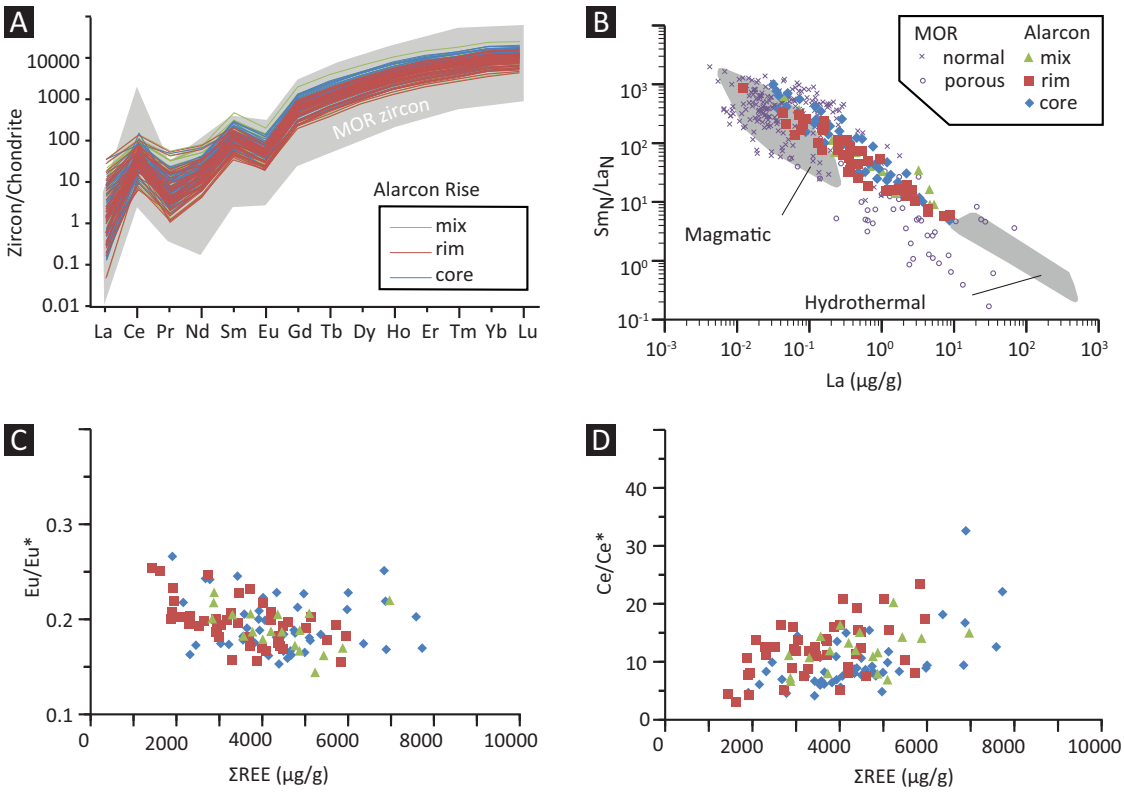

Fig. 9. REE plots for Alarcon Rise zircon ($n = 111$). (A) Chondrite normalized ($_N$) REE concentration diagram showing depleted LREE. Global survey of oceanic zircon from MOR crust after Grimes *et al.* (2009). (B) Comparison of $(Sm/La)_N$ vs La ($\mu g/g$) between zircons from Alarcon Rise and other MOR settings. Normal magmatic MOR zircon exhibits oscillatory to sector zoning (types 1 and 2), whereas porous MOR zircon (type 3) exhibit chaotic zoning patterns with abundant inclusions and pores (Grimes *et al.*, 2009). Discrimination fields for hydrothermal vs magmatic zircon are from continental rocks (Hoskin, 2005). (C) Europium anomaly ($Eu_N/Eu*$) vs total (Σ) REE where Eu* is $Eu_N/\sqrt{(Sm_N \times Gd_N)}$. (D) Cerium anomaly ($Ce_N/Ce*$) vs ΣREE where Ce* is equal to $Ce_N/\sqrt{(La_N(1/3) + Nd_N(2/3))}$. Plot symbols correspond to zircon grain rims (red square/line), cores (blue diamond/line), or mixed regions that included both core and rim (green triangle/line). Core vs rim classification is based on laser spot positions within grain zoning patterns (Fig. 7). Chondrite values are from Sun & McDonough (1989).

nucleate and crystallize at the same time but instead formed over an extended period of magma cooling and fractionation.

Zircon Hf and O isotope geochemistry

Zircon $^{176}Hf/^{177}Hf_{initial}$ (t = 0 Ma) values ranging from 0.283396 to 0.283027 (for grains with $^{176}Yb/^{177}Hf < 0.20$) were calculated using the Lu-decay constant of Scherer *et al.* (2001) and a CHUR value of 0.282785 (Bouvier *et al.*, 2008). Due to the very young age of all zircon grains (Fig. 8) and very long half-life of the Lu-Hf system, $^{176}Hf/^{177}Hf_{initial}$ is indistinguishable from $^{176}Hf/^{177}Hf_{measured}$ making additional corrections for radiogenic decay negligible.

Epsilon hafnium (εHf_{zircon}) data from 80 zircon grains (85 total analyses not including grains with $^{176}Yb/^{177}Hf > 0.20$) from four samples yield a Gaussian distribution with an average of 13.7 ± 5.6 (2σ; Fig. 13A), indicating a normal to enriched DMM source ($\varepsilon Hf_{zircon} = 16.8$–$11.1$; Workman & Hart, 2005). The ±5.6 SD in εHf_{zircon} values of the population is much larger than the average internal analytical error of ±2.4 (2σ) on each measurement. The Gaussian distribution is asymmetric with a notable proportion of grains with relatively lower (more enriched) ε and a much smaller tail of analyses at high (more depleted) ε value. The peak mode is consistent with mantle zircon, but with a wide overall range between $\varepsilon Hf_{zircon} = 19$ and 8, within a 95% CI (Fig. 13A). A subset of zircons with multiple spot analyses in single grains ($n = 14$, including grains with $^{176}Yb/^{177}Hf > 0.20$), confirm generally more variable εHf_{zircon} in grain cores vs rims (Fig. 14A). This variation is within analytical precision for most grains (8/14) but is primarily lower in grain cores that are analytically distinct from grain rims (5/6). Overall variability is most pronounced in grain cores with high $^{176}Yb/^{177}Hf$, which also tend to have larger analytical uncertainty. Higher $^{176}Yb/^{177}Hf$ generally reflects higher overall Yb contents in grain cores (Fig. 14B).

Interference of ^{176}Yb on ^{176}Hf during MC-ICPMS analysis reduces analytical precision, particularly at high Yb concentrations (e.g. Fisher *et al.*, 2014). Due to the high HREE/Hf contents of oceanic zircon, including high Yb in Alarcon zircon, it is important to effectively evaluate the validity of the noted range in reported εHf_{zircon} (Fig. 13A). Including analyses with $^{176}Yb/^{177}Hf > 0.20$ (30/115) in the zircon dataset makes <2% difference to the average εHf_{zircon} (13.5 ± 6.8) but does increase the standard deviation by 1.2ε units. No obvious trends were identified in plots of εHf_{zircon} vs Yb (Fig. 14C), suggesting

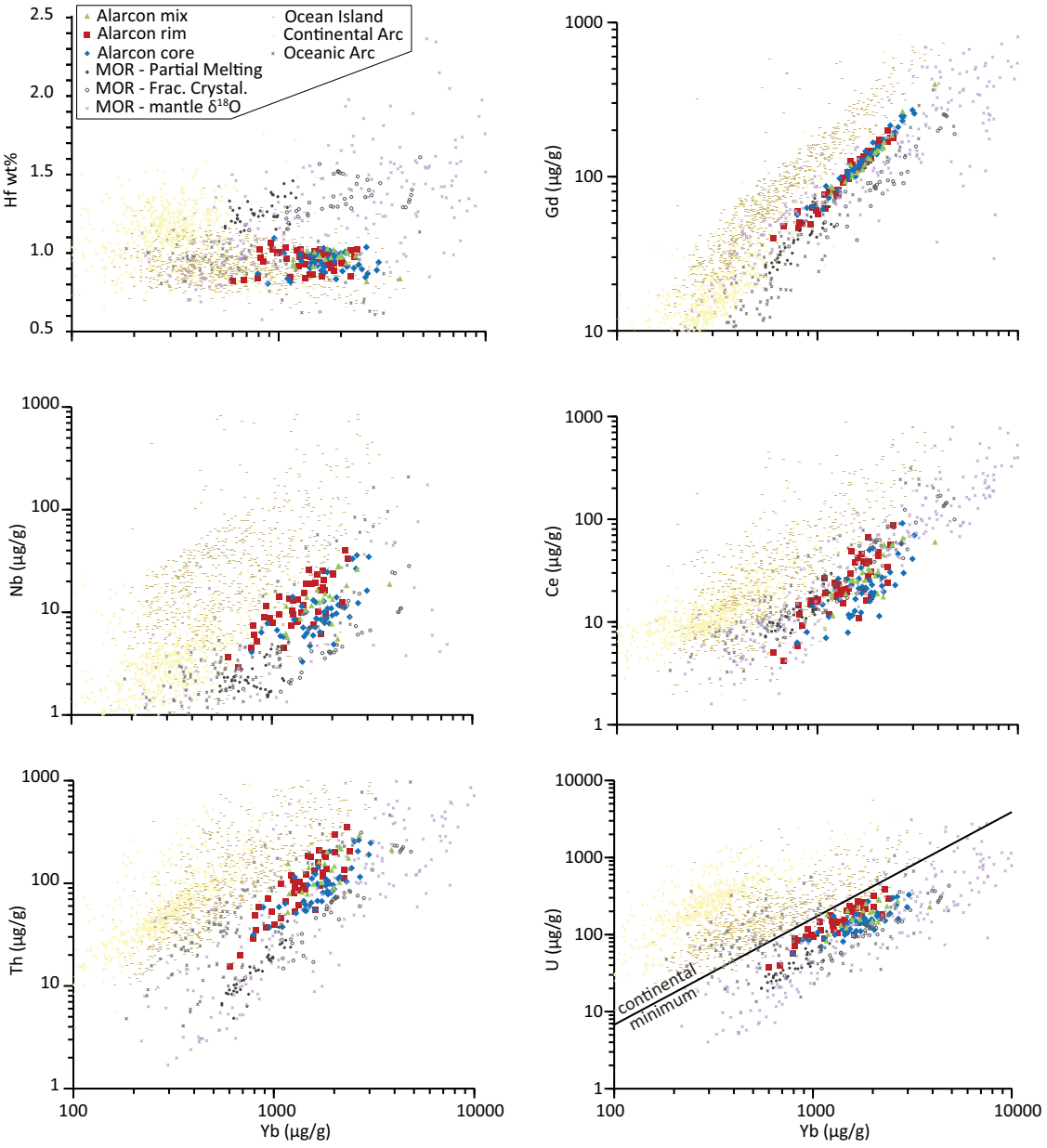

Fig. 10. Zircon trace element diagram of Yb vs Hf, Gd, Nb, Ce, Th, and U. MOR data from Southwest Indian and Mid-Atlantic Ridge zircons are interpreted to have formed from partial melting and fractional crystallization processes (Pietranik *et al.*, 2017) and exhibit mantle-like $\delta^{18}O_{zircon}$ (Grimes *et al.*, 2009, 2011). Ocean Island data from Icelandic rhyolites and North American continental arc data are from Carley *et al.* (2014) and the references therein. Oceanic arc data are from the forearc, back-arc, and remnant arc areas of the Izu-Bonin system (Barth *et al.*, 2017).

that overall high Yb and low Hf (wt%) concentrations in Alarcon Rise zircons cannot explain the wide range of measured εHf_{zircon} alone in grains with <0.20 $^{176}Yb/^{177}Hf$. A minor to negligible impact of the Yb-interference correction on reported εHf_{zircon} is also indicated by a lack of any trend in a plot of the Yb-correction percentage vs εHf_{zircon} (Fig. 14D). This analysis suggests that the large range in Alarcon Rise εHf_{zircon} is mostly natural and not an analytical artifact. This is supported by the much greater 2σ variability across the full dataset (5.6 ε) compared with analytical uncertainty (2.4 ε) alone.

The majority (85/87 grains) of $\delta^{18}O_{zircon}$ measurements fall within a narrow range of 4.6‰–5.5‰ (Fig. 13B). The average $\delta^{18}O_{zircon}$ of 5.0 ± 0.3‰ (n = 87; 2σ) overlaps with the accepted mantle-derived value (5.3 ± 0.3‰; Valley, 2003). Standard deviation of the population (0.45‰) is approximately double the average individual measurement precision (0.27‰) implying some of the range in data is real. No discernable differences were noted in grain cores vs rims or between dark vs light CL domains. Analysis pairs from single grains where both a core and rim were measured have lower $\delta^{18}O_{zircon}$ in 10/19 grains. Alarcon $\delta^{18}O_{zircon}$ is notably higher than the majority of Icelandic rhyolite-hosted zircon thought to form from partial melting of hydrothermally altered crust (2.2‰–4.8‰; Bindeman *et al.*, 2012*a*; Padilla *et al.*, 2016).

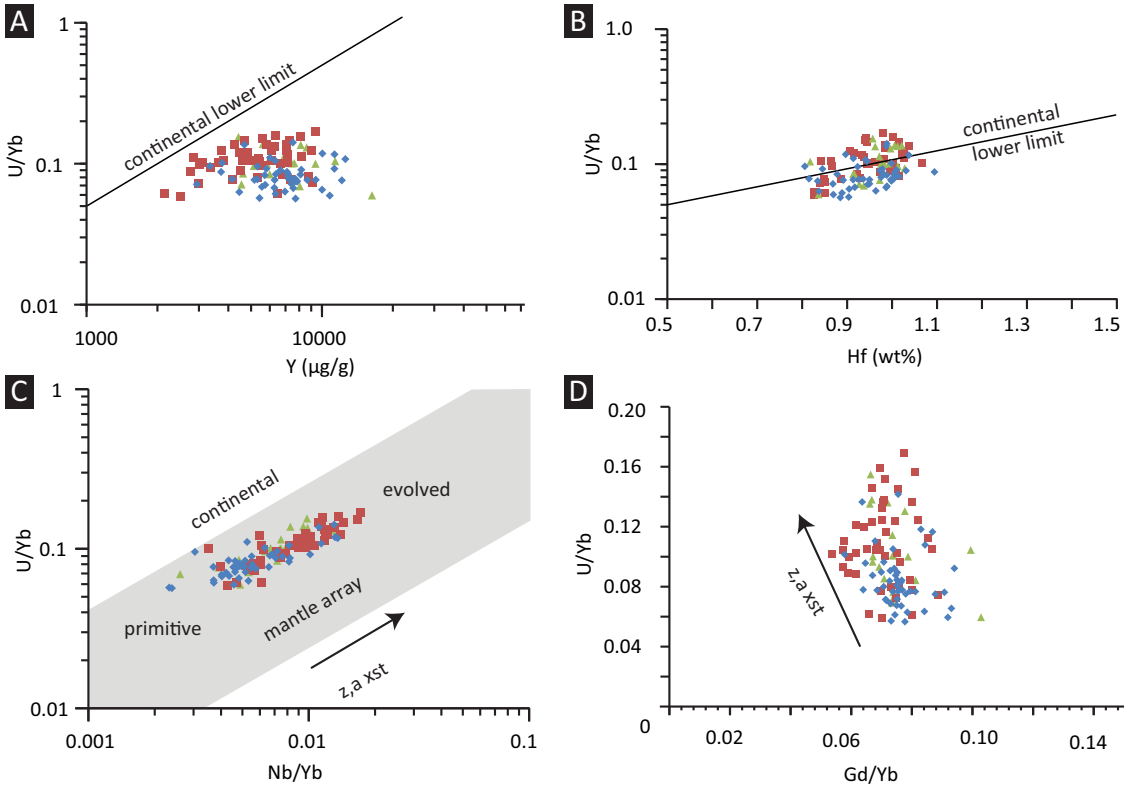

Fig. 11. Zircon trace element discrimination diagrams for Alarcon Rise zircon. Lower limit of continental zircon in A–C is from Grimes *et al.* (2007). Mantle array and vectors for zircon and apatite crystallization (z, a xst) in C and D are from Carley *et al.* (2014) and Grimes *et al.* (2015). Symbols correspond to legends shown in Figs 9 and 10.

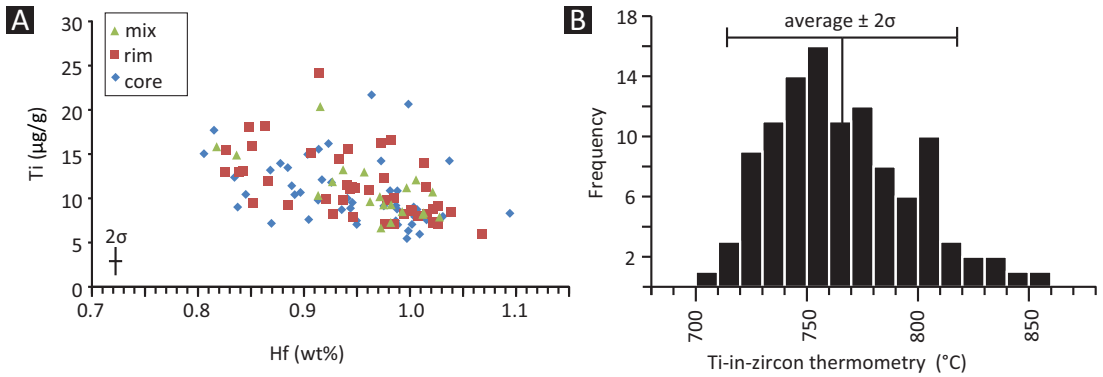

Fig. 12. Titanium (μg/g) and Hf (wt%) concentrations (A) and Ti-in-zircon crystallization temperatures (B) for Alarcon Rise zircons. Increasing Ti correlates with increasing crystallization temperature. Titanium-in-zircon thermometry was calculated using $a_{TiO2} = 0.8$ and $a_{SiO2} = 1.0$ and calibrated for pressure at 4 ± 2 km depth below seafloor (after Ferry & Watson, 2007). Average temperature (vertical bar) and 2σ analytical error (horizontal bar) on each temperature measurement is 52°C.

DISCUSSION

Oceanic MORB mantle source

Little to no contribution from continental crust or mantle

An oceanic mantle origin for all Alarcon Rise lavas is indicated by whole rock Hf-Nd-Sr-Pb isotope geochemistry. Data fall within the existing EPR field and are consistent with a DMM to EDMM affinity (Figs 5 and 6A). Whole rock δD also show good agreement with a normal to slightly enriched Pacific MORB mantle source (Fig. 6C). This conclusion is supported by eruption of both N-MORB and rare E-MORB along Alarcon Rise (Clague *et al.*, 2018).

Trace element concentrations below the minimum values determined for continental crust (Figs 10 and 11) and a relatively juvenile Hf-isotope signature (Fig. 13A) for Alarcon zircon support an oceanic crust affinity and suggest that they are genetically related to their host rhyolitic melt and are not continental xenocrysts (cf. Ashwal *et al.*, 2017). Most εHf_{zircon} data (with $^{176}Yb/^{177}Hf < 0.20$) fall within the oceanic mantle zircon field (Kostitsyn *et al.*, 2009; Portner *et al.*, 2011; Padilla *et al.*, 2016), but some grains exhibit an enriched character (<11 εHf_{zircon}; Fig. 13A). These enriched grains create a broad range in Alarcon εHf_{zircon} at constant

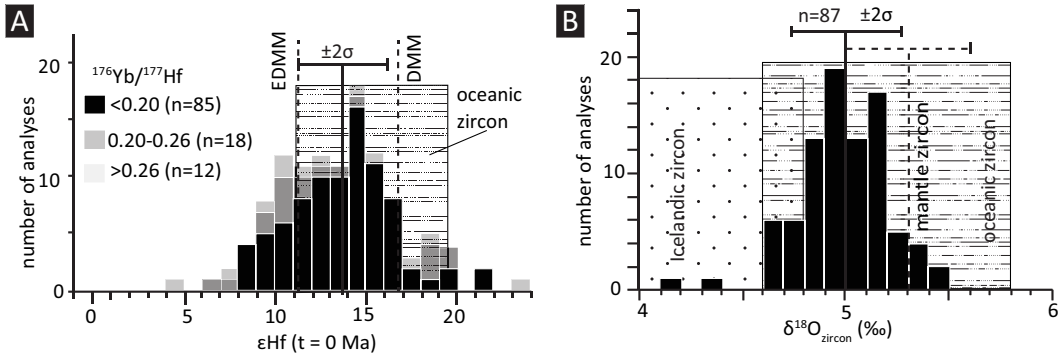

Fig. 13. Alarcon zircon Hf and O isotope data. (A) Stacked column frequency histogram of εHf_{zircon} ($n = 115$). Normal to enriched oceanic zircon field (horizontal dashed pattern) from Kostitsyn *et al.* (2009), Portner *et al.* (2011), Jeffcoat (2012), and Pietranik *et al.* (2017). Ideal DMM and EDMM sources (vertical dashed lines) are from Workman & Hart (2005). Average εHf_{zircon}, for grains with $^{176}Yb/^{177}Hf < 0.20$ is shown by solid vertical line with horizontal $\pm 2\sigma$ analytical error bars. (B) Stacked column frequency histogram of $\delta^{18}O_{zircon}$ ($n = 87$) with average (solid vertical line) and analytical $\pm 2\sigma$ (error bars) values. Average mantle zircon (vertical dashed line) with $\pm 2\sigma$ bars is from Valley (2003). Range of normal oceanic zircon (horizontal dashed pattern) is from Grimes *et al.* (2011). Icelandic zircon field (dotted) is from Padilla *et al.* (2016) and extends to 2.2‰.

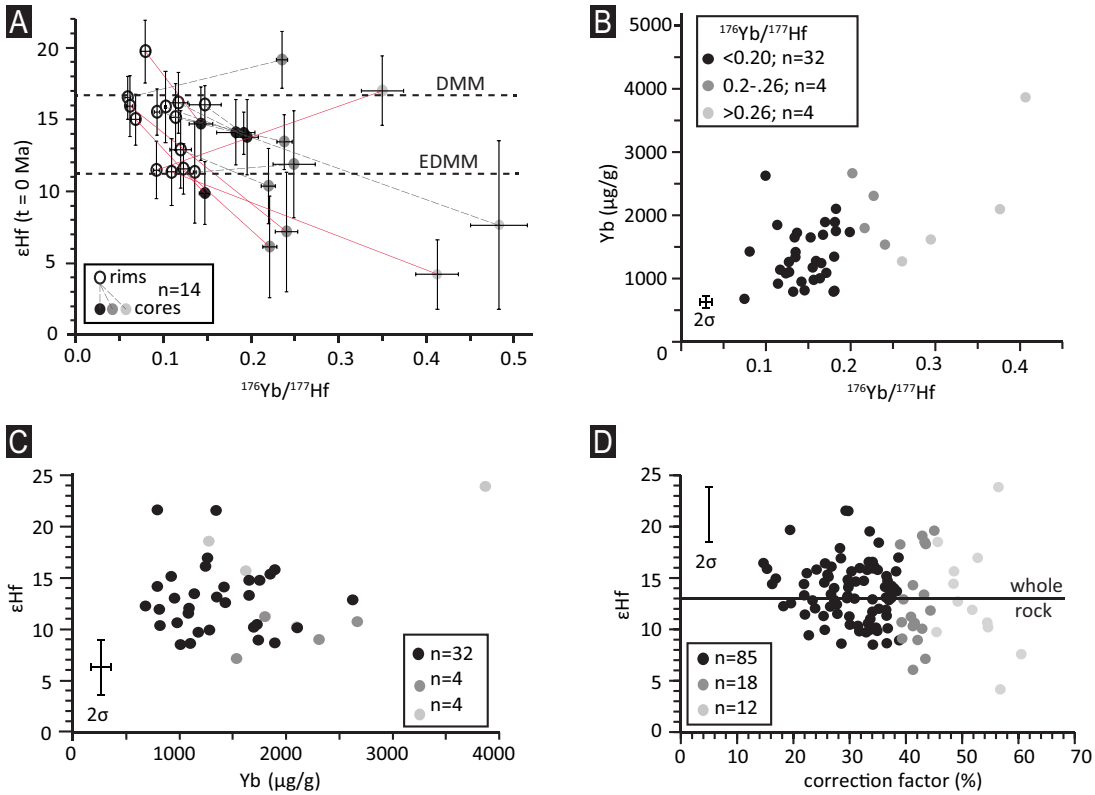

Fig. 14. Plots of Hf and Yb isotope and concentration data from zircon. Samples color coded by $^{176}Yb/^{177}Hf$ values of <0.20 (black), 0.20–0.26 (medium gray), and > 0.26 (light gray). (A) Isotopic comparison of cores and rims from single zircon grains ($n = 14$). Tie-lines connect grains with paired core-rim analyses. Solid red tie-lines indicate grains with analytically distinguishable core-rim variation, whereas dashed tie-lines connect paired analyses that are within analytical 2σ error. Mantle source reservoirs (DMM and EDMM) are from Workman & Hart (2005). (B) Yb^{176}/Hf^{177} and total Yb concentrations collected by MC-ICPMS and LA-ICPMS analysis, respectively, from different spots on single grains. Two-σ analytical error is smaller than the size of the plotted points. (C) Hf isotopic values from MC-ICPMS compared with total Yb concentration (LA-ICPMS), collected from different spots on single grains. (D) Hf isotopic values (εHf_{zircon}) vs Yb correction factors. The Yb correction factor = $(^{176}Hf/^{177}Hf_{measured} - {}^{176}Hf/^{177}Hf_{corrected})/{}^{176}Hf/^{177}Hf_{measured}$ is directly proportional to $^{176}Yb/^{177}Hf$, where the 0.20% cutoff used in other plots corresponds to a 42% correction. The solid line represents the average whole rock εHf (Fig. 6A).

$\delta^{18}O_{zircon}$ that falls within a 0%–5% mixing model domain between southern Baja continental crust and DMM (Fig. 15). However, the most enriched zircons are still within analytical uncertainty (~2.4 ε units) of an EDMM source reservoir and do not require any continental input to explain their composition. This point is supported by zircon trace element patterns that show very little to no continental signature in multiple discrimination plots. Although we cannot preclude a minor contribution of continental crust, combined observations from zircon trace element and isotope geochemistry suggest that nearby Mexican crust was likely not involved in formation of Alarcon Rise rhyolites despite its proximity.

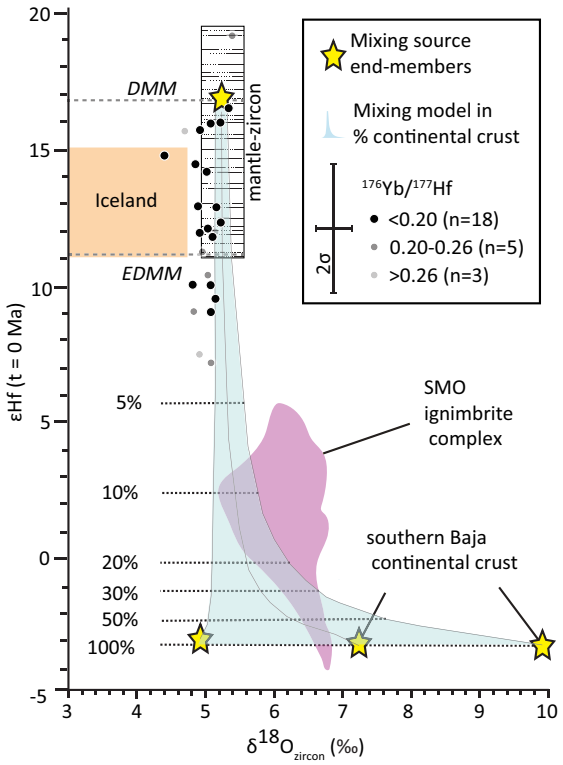

Fig. 15. Zircon Hf vs O isotope plot showing mixing domain (light blue) between zircon formed from hypothetical source reservoirs (stars). Data from the SMO ignimbrite field in western mainland Mexico are from Andrews *et al.* (2014). Mixing line end-member εHf, and O and Hf concentrations are from Workman and Hart (2005; DMM) and Schaaf *et al.* (2000, continental crust). Continental crust εHf values were converted from εNd using the terrestrial array of Vervoort *et al.* (2011) and correspond to granitoids exposed on the LCB of the southern Baja Peninsula (see LCB in Fig. 1B). End-member $\delta^{18}O$ values for zircon from DMM and a likely range of continental crust sources are from Bindeman (2008) and Valley *et al.* (2005), respectively. Zircon εHf and $\delta^{18}O$‰ values from Icelandic rhyolites represent a hydrothermally altered oceanic crust affinity (Bindeman *et al.*, 2012*a*; Padilla *et al.*, 2016).

Zircon Hf isotopic heterogeneity

The few studies of εHf_{zircon} from MOR crust show that single sample sites tend to vary by 9 to 4 ε units (Kostitsyn *et al.*, 2009; Portner *et al.*, 2011; Jeffcoat, 2012; Thomas, 2013; Padilla *et al.*, 2016), which is generally much less than Alarcon rhyolite εHf_{zircon} (~11 ε units). Alarcon's large range is comparable to $\varepsilon Hf_{wholerock}$ variation measured from the full length of the EPR (17.7 to 6.0) or the Mid-Atlantic Ridge (18.6 to 9.8; Nowell *et al.*, 1998; Salters *et al.*, 2011, Zhang *et al.*, 2016). In sum, the full range of εHf_{zircon} seen in Alarcon Rise rhyolites (19 to 8) is nearly equivalent to the full $\varepsilon Hf_{wholerock}$ range of MOR oceanic crust in general. Below, we suggest that this is likely due to the high sensitivity of zircon in capturing εHf that would otherwise be overlooked in whole rock studies.

Although some of the variability in Alarcon εHf_{zircon} corresponds with higher overall Yb in grain cores, analysis of the Yb-interference correction supports the interpretation that most of the observed range is real (Fig. 14D). This is important since the whole rock dissolution method generally minimizes Yb-interference and $\varepsilon Hf_{wholerock}$ (13.07 ± 0.13, $n = 5$) is strikingly more precise than εHf_{zircon} (13.7 ± 5.6, $n = 85$). Discrepancies between whole rock and zircon εHf can be related to variability between zircon and other phases digested during whole rock analysis (e.g. Tang *et al.*, 2014; Huang *et al.*, 2019), but close similarity between average $\varepsilon Hf_{wholerock}$ and εHf_{zircon} from Alarcon Rise suggest this is unlikely. Rather, it is more plausible that the $\varepsilon Hf_{wholerock}$ signal homogenizes the range recorded by εHf_{zircon}. This may be due to εHf_{zircon} variability primarily coming from zircon cores, which make up a relatively insignificant volume of material that would contribute to $\varepsilon Hf_{wholerock}$. Importantly, the EDMM-DMM range preserved by εHf_{zircon} is corroborated by whole rock Pb isotopes that also range from enriched to normal DMM source end-members (Fig. 5B and C).

The εHf_{zircon} variability seen in Alarcon rhyolite is not uncommon for granitoids from the continental crust. Variability of 10–11 ε units for individual granite samples require magma-mixing from different sources of melt generation and pluton emplacement, over millions of years in some cases (e.g. Kemp *et al.*, 2007; Yang *et al.*, 2007; Shaw & Flood, 2009). In general, researchers studying continental rocks rely on zircon, vs whole rock, to identify isotopic end-members and assess the magnitudes of their input during magma petrogenesis. Within this context, Alarcon Rise zircon likely preserves the melting of a heterogeneously enriched mantle source that replenished an evolving MORB magma over tens of thousands of years of rhyolite petrogenesis.

Magma evolution

Zircon growth history

U-series geochronology shows that the vast majority of Alarcon Rise zircons crystallized by ~23 ka. These ages are much younger than nearby Mexican continental crust (>5 Ma; Ferrari *et al.*, 2007; Fletcher *et al.*, 2007), supporting the interpretation that Alarcon grains are not continental xenocrysts. The older Alarcon grain population (~45 ka), however, indicates a complicated history of rhyolite petrogenesis and zircon crystallization that generated textural and chemical differences between core and rim.

Grain-scale variations in zircon trace elements from core to rim record chemical changes in the host melt with time (e.g. Claiborne *et al.*, 2006) and can be used to interpret rhyolite magma evolution on Alarcon Rise. Previous work has suggested that increasing oceanic zircon U/Yb toward more 'continental-like' compositions may be caused by low degrees of partial melting or influence of a more enriched MORB mantle source (Portner *et al.*, 2011). Similar εHf in zircon grain cores compared with rims (Fig. 14A) would then suggest that progressive depletion of Yb relative to U in grain rims is caused by magma fractionation processes and not changes in source enrichment. This interpretation is also supported by increasing Nb/Yb from grain cores to rims (Fig. 11C),

which can be produced by apatite and zircon fractionation during magma evolution (Grimes *et al.*, 2015). Moreover, slightly higher ΣREE in grain cores, primarily by early uptake of less incompatible HREE, would deplete the residual melt in REE from which later grain rims would crystallize. Some overlap in these chemical signals between grain cores and rims, however, may indicate periodic recharge events of more primitive magma that mixed with the zircon magma host.

Trace element chemical variation is also displayed by darker CL cores and brighter CL rims for the majority of grains. Although most grains (>70%) show relatively clean oscillatory and sector zoning from core to rim, evidence for continuous chemical evolution, a noticeable small subpopulation shows abrupt contacts and changes in zoning patterns at the core-rim boundary. Anhedral and/or porous to pitted cores (Fig. 7E and F) in the small subpopulation represent a more complex growth history that reflects a change in the chemical environment from which some grains grew.

Porous/pitted zircons representing a small portion of grains collected from the plutonic section of MOR crust (Grimes *et al.*, 2009) have been interpreted to form in the presence of aqueous solutions. Such fluids are invoked to be necessary in the generation of many MOR silicic magmas (i.e. plagiogranites), which have largely been interpreted to form through assimilation of hydrated oceanic crust and subsequent fractional crystallization (AFC; e.g. Wanless *et al.*, 2010). This process is often indicated by lower $\delta^{18}O$ values than expected from crystal fractionation alone (Bindeman *et al.*, 2012*a*; Hampton *et al.*, 2021). Although sharp boundaries between textural domains of some Alarcon zircon exist, their $\delta^{18}O_{zircon}$ signature of $5.0 \pm 0.3‰$ is more representative of a juvenile DMM source ($\delta^{18}O_{zircon} = 5.3 \pm 0.3‰$; Valley, 2003) without the need for assimilating hydrated oceanic crust. Zircon grains with porous microstructure may also form during dissolution-precipitation processes (Halpin *et al.*, 2020), which could explain anhedral core-rim boundaries. This latter process would likely accompany periodic mafic recharge events over ~20 kyr of rhyolite petrogenesis.

Rhyolite petrogenesis

Fractional crystallization may account for the production of some high silica magmas on the MOR (Byerly, 1980; Juster *et al.*, 1989; Geist *et al.*, 1995) and back-arc spreading centers (Beier *et al.*, 2015), but other mechanisms including liquid immiscibility (Charlier *et al.*, 2013), gabbro/sheeted dike partial melting (France *et al.*, 2010; Grimes *et al.*, 2013), and AFC involving seawater-altered oceanic crust (Gerlach *et al.*, 1981; Oskarsson *et al.*, 1982; Pedersen & Malpas, 1984; Nicholson *et al.*, 1991; Haase *et al.*, 2005; Wanless *et al.*, 2010; Van Der Zander *et al.*, 2010) or hydrothermal brines (Michael & Schilling, 1989; Jeanvoine *et al.*, 2021) have been proposed to occur. Experiments and sampling generally show that liquid immiscibility produces mafic, including FeTi basalt, and felsic end-members, without a significant proportion of intermediate composition (52–65 wt% SiO_2) magmas (Dixon & Rutherford, 1979; Charlier *et al.*, 2013). The abundance of intermediate lava flows and minor amount (by volume) of felsic lava flows on Alarcon Rise likely rules out liquid immiscibility (Figs 1D and 2). Instead, major element trends are more consistent with a fractional crystallization model that includes some hybridization (mixing) between intermediate and end-member compositions (Clague *et al.*, 2018; Fig. 3). However, the cited model also does not match measured trends in Cl and K_2O, which are much more enriched than simple fractionation models (Fig. 16A). Elevated Cl is generally ascribed to surface to subsurface contamination by hydrothermal brines or assimilation of seawater-altered crust around the margins of evolving magma bodies in magmatic arc, hotspot, and MOR settings (Michael & Cornell, 1998; Perfit *et al.*, 2003; le Roux *et al.*, 2006; Wanless *et al.*, 2010; Deardorff *et al.*, 2011; Portner *et al.*, 2014; Hampton *et al.*, 2021; Jeanvoine *et al.*, 2021).

Assimilation of hydrothermally altered lower oceanic crust

Determining whether the petrogenesis of evolved MOR magmas requires the involvement of seawater-altered mafic crust, through bulk assimilation or addition of small percentage partial melts, has largely hinged on the identification of geochemical signals predicted by experimental and numerical models (e.g. Dixon & Rutherford, 1979; Juster *et al.*, 1989; Berndt *et al.*, 2004; Koepke *et al.*, 2004). Major elements trends, particularly that of Ti, from partial melting experiments of gabbro and sheeted dike samples show promise but diverge under different run conditions and are inconclusive (Koepke *et al.*, 2007; France *et al.*, 2010). Partial melts derived from hydrous oceanic crust can also be identified from whole rock trace element concentrations where La and Yb remain constant with increasing SiO_2 (Brophy, 2009). A similar origin is interpreted for zircon with lower Nb, Ce, Gd, Th, and Yb (Pietranik *et al.*, 2017). Enrichment of these elements in Alarcon Rise zircon (Fig. 10) instead supports a fractional crystallization origin for their host rhyolites without the need for crustal assimilation. However, comparably large ranges in said trace elements in MOR zircon that lack (Grimes *et al.*, 2011) or contain (Carley *et al.*, 2014) evidence for assimilation of hydrous oceanic crust question their utility as an effective petrogenetic discriminator. Rather, more reliable interpretations can be drawn from combined trace element and isotope investigations of zircon and whole rock/glass geochemistry, particularly $\delta^{18}O$ data (e.g. Bindeman, 2008; Grimes *et al.*, 2011, 2013; Padilla *et al.*, 2016).

Direct measurement and modeled trends show that $\delta^{18}O$ variation during fractionation from basalt to rhyolite can increase by 0.5‰–1.5‰ (Muehlenbachs & Byerly, 1982; Bindeman, 2008). However, modeled $\delta^{18}O$ fractionation trends are quite variable and highly dependent on mineral crystallization and temperature (Fig. 6B). Compared with wetter and colder calc-alkaline systems, drier

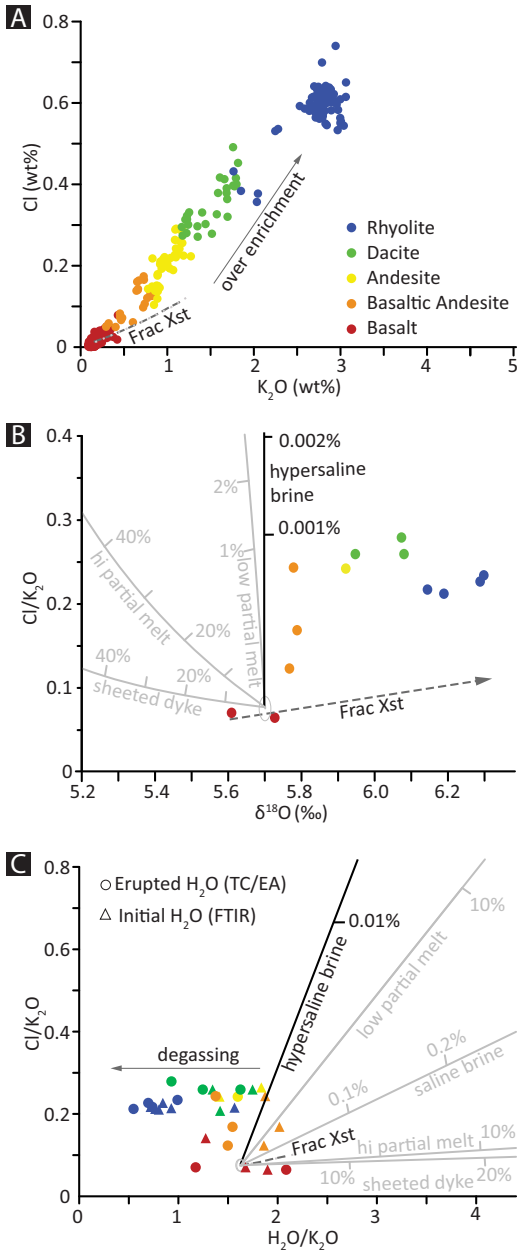

Fig. 16. Contaminant/assimilant identification diagrams. (A) Chlorine vs K_2O electron microprobe glass data for the entire Alarcon Rise (Clague *et al.*, 2018). Fractional crystallization (Frac Xst) models are the same as in Fig. 3 where the high K_2O end of the trend marks the predicted most siliceous composition. (B) Whole rock $\delta^{18}O$ data (Fig. 6B) vs microprobe glass Cl/K_2O data. Mixing lines (gray and black solid lines) connect primitive basalt (empty gray circle) with three end-members: (1) hypersaline brine (50% NaCl; Kent *et al.*, 1999), (2) sheeted dikes exhibiting <50% alteration between 1500 and 2000 mbsf in OSDP hole 504B (Sparks, 1995; Zuleger *et al.*, 1995), and (3) low (1%) and high degree (20%) partial melts from the sheeted dike composition. Partial melts were modeled using Rhyolite-MELTS at QFM-M1 and 100 MPa (Gualda *et al.*, 2012). End-member $\delta^{18}O = 4.61‰$ for sheeted dike (Alt *et al.*, 1995) and their partial melts, and $\delta^{18}O = 0.85‰$ for the hypersaline brine (Alt *et al.*, 2010). Fractional crystallization $\delta^{18}O$ values are from Bindeman (2008; Fig. 6B) and Cl/K_2O from Rhyolite-MELTS output (see Fig. 3 caption). All mixing lines calculated after Ersoy & Helvaci (2010), with tick marks corresponding to relative percentages of end-members needed to mix with the starting basalt. (C) Chlorine/K_2O vs H_2O/K_2O contaminant/assimilant mixing diagram. Saline (15% NaCl) brine component composition is from Kent *et al.* (1999), whereas the sources of the other components are the same as in B. Erupted H_2O (circles) measured with TC/EA, and initial (undegassed) H_2O (triangles) calculated from published FTIR data (Fig. 6D).

and hotter tholeiitic systems, like Alarcon Rise (Fig. 3) should generate overall lower increases in $\delta^{18}O$ of ~1‰ (Bucholz *et al.*, 2017). Lower than expected $\delta^{18}O_{wholerock}$ measurements, compared with modeled trends, in MOR dacites and rhyodacites have led many to invoke assimilation of hydrated oceanic crust during their petrogenesis (e.g. Perfit *et al.*, 1999; Wanless *et al.*, 2011). A similar interpretation has been extended to ophiolitic plagiogranites using calculated melt $\delta^{18}O$ compositions for the melt from which zircon grew ($\delta^{18}O_{calc\text{-}melt}$; Grimes *et al.*, 2013; Morag *et al.*, 2020). However, below, we show that this process is not required to produce the geochemical signature of Alarcon Rise rhyolites.

Alarcon zircon $\delta^{18}O_{calc\text{-}melt}$ of $6.7 \pm 0.5‰$, calculated after Bucholz *et al.* (2017) using major element compositions (Clague *et al.*, 2018) and Ti-in-zircon crystallization temperatures, extend to higher values than rhyolite $\delta^{18}O_{wholerock}$ ($6.2 \pm 0.2‰$). These values are ~0.6‰–1.1‰ higher than basaltic $\delta^{18}O_{wholerock}$ and within the expected range of high silica magmas formed solely from crystal fractionation of MORB or high-Mg arc basalt (see MORB and normal $\delta^{18}O$ arrays in Fig. 6B). A MORB protolith for rhyolite $\delta^{18}O_{calc\text{-}melt}$ reflects average $\delta^{18}O_{zircon}$ ($5.0 \pm 0.3‰$), which is analytically indistinguishable from mantle-like zircon ($5.3 \pm 0.3‰$; Valley, 2003) and modern normal MOR plutonic crust thought to have crystallized in a closed system ($5.2 \pm 0.5‰$; Grimes *et al.*, 2011). This observation suggests that little if any assimilation of seawater-hydrated oceanic crust was required during differentiation of Alarcon MORB to rhyolite and prior to zircon crystallization.

Secondary processes during magma ascent and eruption

Although $\delta^{18}O_{calc\text{-}melt}$ and $\delta^{18}O_{wholerock}$ are within analytical uncertainty, the latter is consistently lower than most model trends (Fig. 6B). This might reflect incorporation of low $\delta^{18}O$ mafic minerals (e.g. pyroxene>olivine>>FeTi oxides) into the rhyolite magma. Abundant crystalline basalt xenoliths (Fig. 4A and B), and zoned clinopyroxene and plagioclase phenocrysts with mafic affinities (Dreyer *et al.*, 2014) would lower the $\delta^{18}O_{wholerock}$ signal compared with $\delta^{18}O_{calc\text{-}melt}$. The presence of these mafic materials within rhyolite samples, as well as the occurrence of hybrid lavas (Fig. 3), suggests that incorporation of wall rock during magma ascent and/or magma-mixing was important during development of the Alarcon lava suite (Clague *et al.*, 2018) and could have produced the small disparity between rhyolite $\delta^{18}O_{calc\text{-}melt}$ and $\delta^{18}O_{wholerock}$. Future mineral chemistry data will determine what proportion of the rhyolite crystal cargo is mafic and if it could effectively lower the $\delta^{18}O_{wholerock}$ signal.

Another explanation for the disparity between $\delta^{18}O_{calc\text{-}melt}$ and $\delta^{18}O_{wholerock}$ could be attributed to seawater assimilation subsequent to zircon crystallization. Volatile speciation data from FTIR analysis indicate that Alarcon Rise rhyolite glasses with >>2.5 wt% H_2O_t preserve syn- or post-eruptive hydration (Portner *et al.*, 2021), a trait that might be shared by one sample used for

$\delta^{18}O_{wholerock}$ analysis with unusually high H_2O (2.5 wt%; Fig. 6D). High temperature (>300°C) diffusion of seawater ($\delta^{18}O = -0.1$ to -0.3; Keigwin, 2002) into the glass matrix during or shortly after eruption could lower $\delta^{18}O_{wholerock}$, but the co-occurring zircon ($\delta^{18}O_{calc\text{-}melt}$) would be left unaffected and reflect the pristine DMM source. Evidence for this process is preserved by Cl- and H_2O-enriched flow bands in some MORB lavas and Alarcon rhyolite samples (Portner *et al.*, 2014, 2015). This interpretation would suggest that slightly lower $\delta^{18}O_{wholerock}$ compared with $\delta^{18}O_{calc\text{-}melt}$ may just be an artifact of syn-eruptive hydration. Moreover, although models for entrainment of mafic material and/or secondary hydration during magma ascent and eruption may explain the minor discrepancy between $\delta^{18}O_{wholerock}$ vs $\delta^{18}O_{calc\text{-}melt}$, they do not explain Cl and K over enrichment observed in all evolved lava compositions erupted alongside the rhyolite dome (Fig. 16A).

Deep-seated contamination by hydrothermal brines

Incorporation of a Cl-enriched component without greatly modifying $\delta^{18}O$ is possible through contamination by minimal amounts of hypersaline brine (Fig. 16B). Phase separation of hydrothermal cells in the oceanic crust can produce hypersaline brines with ~50 wt% NaCl near the top of axial melt lenses and low salinity fluids that vent from black smoker vent fields at the surface (Fig. 17A; Nehlig, 1991; Kelley & Früh-Green, 2001; Coumou *et al.*, 2009). Deep-seated hypersaline brines are a primary contaminant source for unusually Cl-rich fractionated basalts and more evolved lavas in MOR, back-arc, and oceanic island settings (Michael & Shilling, 1989; Kent *et al.*, 1999; Jeanvoine *et al.*, 2021). Up to 95% and 40% of the Cl and H_2O, respectively, in submarine glasses may ultimately be derived from contamination by hypersaline brine early on during magma evolution (Kendrick *et al.*, 2013).

Other potential sources of Cl enrichment from bulk assimilation of altered lower crust (e.g. sheeted dikes) or their partial melts would produce lower $\delta^{18}O$ and higher H_2O/K_2O than observed in Alarcon lavas (Fig. 16B and C). Although low degree (1%) partial melts of an altered mafic crustal component may achieve similar Cl/K_2O contents to observed sample trends (e.g. Wanless *et al.*, 2011), such a low percentage of partial melt falls below the threshold for effective melt segregation and migration (Vigneresse *et al.*, 1996; Lee & Morton, 2015) unless significant fracturing/deformation can provide pathways for melt migration (Etheridge *et al.*, 2020). Higher degrees (20%) of partial melt (andesite in composition) extracted from altered sheeted dikes would be more capable of migrating into an adjacent magma body, but the resulting Cl-enrichment and $\delta^{18}O$ would be far too low compared with what is observed in Alarcon lavas (Fig. 16C). In either case, the assimilation of such crustal components would require a much higher volume of assimilant (>1000X) that is unrealistic (Michael & Shilling, 1989).

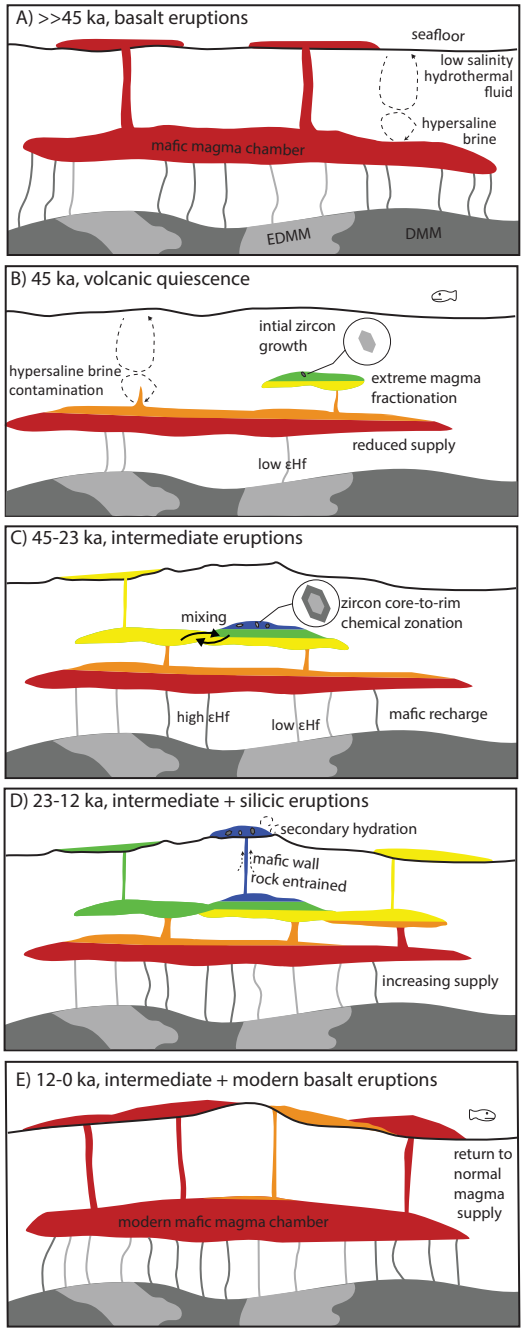

Fig. 17. Cartoon showing time-steps for the evolution and eruption of evolved lavas on Alarcon Rise. Mafic to felsic magma compositions represented by hot (red) to cool (blue) colors, respectively (see color spectrum in Fig. 16). Relative magma chamber depth in crust is approximate and based on data from spreading ridges (Arnulf *et al.*, 2014) with intermediate-rates (~50 mm/yr) and normal oceanic crustal thickness (6–7 km) like Alarcon Rise (Lizarralde *et al.*, 2007; DeMets *et al.*, 2010). Magma chamber thicknesses and inner stratification are not drawn to scale. (A) > > 45 ka: normal magmatic spreading conditions with high magma flux sourced from a heterogeneously enriched Pacific MORB mantle source (light to dark gray). (B) ~45 ka: decreased magma supply during a period of amagmatic extension initiates, causing magma chambers to stagnate and differentiate to more evolved compositions. (C) 45–23 ka: small recharge events over 22 kyr allow isotopically diverse magmas to mix and fractionate, producing a wide range in zircon εHf. Initial eruptions of more evolved compositions occur. (D) 23–12 ka: zircon crystallization ceased by this time. Increasing magma flux triggers eruptions of silicic and intermediate lavas at the surface. (E) < 12 ka: magma flux continues to increase until normal magmatic spreading conditions return with voluminous basalt eruptions at the surface.

Higher volumes of assimilant would also enrich the magma in H_2O, but average initial H_2O contents in rhyolite at 100 MPa calculated from dissolved and exsolved components (Fig. 6D) closely match predicted H_2O contents from fractional crystallization. Although relatively lower H_2O/K_2O in the more evolved Alarcon Rise magmas could be explained by degassing processes (e.g. Wanless *et al.*, 2010), samples generally converge along the hypersaline brine mixing line (Fig. 16C). Thus, overall, increasing Cl/K_2O from basalt to basaltic andesite and constant Cl/K_2O in more evolved lavas suggest that hypersaline brine contamination occurred early on in the fractionation process (Fig. 16B).

We envisage a model where deep-seated hydrothermal brines interacted with early evolved melts as they migrated from deep to shallower storage levels (see below; Fig. 17B). This process did not trigger or influence rhyolite formation to any great degree and is a common phenomenon along the MOR system (Michael & Schilling, 1989). Following extreme crystal fractionation (Fig. 17C), rhyolitic magma incorporated a small component of low $\delta^{18}O$ wall rock and/or seawater along the conduit during magma ascent and/or in the eruptive vent (Fig. 17D). This interpretation is consistent with models for subsolidus seawater infiltration, alteration, and assimilation along deep-seated crustal fractures after silicic magma petrogenesis (Gillis, 1995; Grimes *et al.*, 2011). Future trace element, isotopic, and melt inclusion volatile studies are needed to better understand high-temperature interaction between brines and seawater with ascending magmas just above the melt lens and in the eruptive conduit and vent environments.

Tectono-magmatic model

Alarcon zircon geochronology, geochemistry, and internal CL-patterns indicate growth and chemical evolution from ~45 to 23 ka. Lower magma recharge during this time could allow differentiation of MORB to rhyolite (Fig. 17B and C). Such evolved oceanic rocks have been proposed to form in magma chambers that are cut-off from their sources during periodic reductions in magma supply (Wanless *et al.*, 2010). The process would likely accompany time periods or spatial focusing of amagmatic vs magmatic extension along intermediate spreading ridges, which has been proposed to explain abyssal hill fabric on Alarcon Rise (Le Saout *et al.*, 2019).

An association of increased tectonic deformation with magma-starved slow-spreading centers suggests that extension in these settings is accommodated by faulting rather than by dike emplacement (Buck *et al.*, 2005; Ito & Behn, 2008). A lower magma supply during eruption of Alarcon rhyolites is supported by a higher occurrence of faults in the northern portion of the spreading segment where they erupted (Fig. 2). The difference between the two zircon age populations suggest that a reduced magma supply may have been sustained for a period of at least ~22 kyr. This extended period of time could have allowed small magmatic pulses from an isotopically variable MORB mantle to ascend and stall in the crust where they would slowly mix and fractionate to eventually produce an eruptible batch of rhyolite magma (Fig. 17C).

Magma recharge, although limited, would need to have been sustained over the 22 kyr of rhyolite evolution to provide enough heat to prohibit complete crystallization. Moreover, silicic melt extraction would be hindered by high crystal contents and, hence, higher viscosity as well as low porosities generated during extreme crystal fractionation from MORB to rhyolite. Modeling (Fig. 3; Clague *et al.*, 2018) shows that the starting MORB liquid must have fractionated >90% crystals in order to evolve to a 74 wt% SiO_2 melt. Such high crystal contents are beyond the terminal porosity (~25%) needed for effective silicic melt extraction (Vigneresse *et al.*, 1996; Lee & Morton, 2015). Therefore, we envisage a multi-tiered magma ascent and fractionation process where the primary MORB magmas evolved to a basaltic andesite melt and residual crystal mush bearing >50% solids in a deep magma chamber (Fig. 17B). Continued magma recharge from below would trigger ascent of the evolved basaltic andesite to a shallower magma lens where it would further fractionate another ≤75% crystals in one or more depth stages. During this initial ascent phase, the early evolved melts would interact with minor amounts of hypersaline brines just above the deep magma chamber.

A step-wise crystal fractionation process is supported by relatively increasing crystal-contents with SiO_2 in intermediate lavas that erupted alongside crystal-rich rhyolite lavas (Portner *et al.*, 2021). Periodic replenishment and mixing of low-SiO_2 intermediate composition magma into a shallow melt lens bearing higher SiO_2 magma would be possible due to similar viscosities, compared with mixing the most mafic and felsic end-members alone (Manga, 1996). Such a punctuated recharge, mixing and differentiation process might explain the presence of 'hybrid' lavas on Alarcon Rise (Fig. 3; Clague *et al.*, 2018) and diverse εHf_{zircon} signal (Fig. 13A). Future analysis and modeling of mineral, melt inclusion, and glass trace element geochemistry will help address this question.

A high abundance of intermediate lavas relative to rhyolites, and a minor proportion of old zircon grains further support the idea that magma recharge was continuous enough to sustain an intermediate composition magma lens, and too hot to allow significant zircon crystallization in rhyolite melt early on (Fig. 17B). Numerical modeling shows that a 25 m thick silicic liquid could develop at the top of a fractionating magma chamber over 22 kyr if it was water saturated (Lee *et al.*, 2015). High initial water contents (4.5–2.0 wt%) estimated for Alarcon rhyolites at depth in the crust prior to magma ascent and degassing would produce low enough viscosities ($10^{5–6}$ Pa s) to allow extraction of a rhyolitic batch equal in volume to lava domes on the seafloor (2–5 × 10^6 m^3; Portner *et al.*, 2021).

The erupted central rhyolite dome volume would have ultimately been generated from up to 10^8 m^3 of mafic magma considering the required ~95% crystal fractionation needed for differentiation. Assuming a steady input over 22 kyr, a resupply rate of 4.5×10^3 m^3/yr would be required for the central Alarcon Rise rhyolite dome source, which is comparable to the lowest eruption rates inferred for the northern EPR (Sinton *et al.*, 2002). Increased magma recharge on Alarcon Rise after 23 ka could then trigger the eruption of silicic lava at the roof of the shallow magma lens (Fig. 17D). This eruption must have been older than ~12 ka, which is the age of the oldest sediment that contains rhyolite ash (Clague *et al.*, 2018). Continued increase in magma supply after 12 ka, closer to typical rates (10^4 m^3/yr over 1 km spreading segment length) inferred for intermediate spreading ridges (White *et al.*, 2006), supported a return to normal basalt dominated volcanism occurring today (Fig. 17E).

CONCLUSIONS

Zircon and whole rock geochemistry of the Alarcon Rise evolved volcanic suite exhibit normal to slightly enriched MOR oceanic crust geochemical signatures. Little to no evidence exists for the incorporation of nearby continental lithosphere or hydrated oceanic crust during rhyolite petrogenesis. Zircon geochronology, geochemistry, and textural characteristics suggest that rhyolite primarily formed between 45 and 23 ka during a time of reduced magma flux, mixing, and differentiation. Increased mantle melting after this period triggered the ascent and eruption of evolved lavas. Alarcon Rise rhyolites are the most evolved volcanic rocks yet found along a normal submarine MOR system away from hot-spots and provide an example of extreme MORB fractionation without crustal assimilation.

ACKNOWLEDGEMENTS

The authors appreciate the extended efforts of many colleagues. The entire ship and ROV crew of the 2012 and 2015 cruises to the Gulf of California supported by the Monterey Bay Aquarium Research Institute (MBARI). Yoann Greau, Elena Belousova, Will Powell, and Steve Craven assisted with zircon sample preparation and analysis. Ilya Bindeman prepared and analyzed samples for whole rock oxygen and hydrogen analysis. Matthew Coble is thanked for assistance with SHRIMP-RG analyses. Kouki Kitajima, Noriko Kita, and John Valley provided technical assistance at WiscSIMS. Jenny Paduan and Dave Caress processed AUV data. Jonathan Miller provided important comments that improved an earlier version of this manuscript. This is contribution 1733 from the ARC Centre of Excellence for Core to Crust Fluid Systems (http://www.ccfs.mq.edu.au) and 1502 in the GEMOC Key Centre (http://www.gemoc.mq.edu.au).

FUNDING

MBARI cruises and DAC were funded by an annual grant from the David and Lucile Packard Foundation; additional funds were provided by National Science Foundation (OCE-1355436 and OCE-1610800 to R.A.P., OCE-1354167 to B.M.D.). The Hf-isotope data were obtained using instrumentation funded by DEST Systemic Infrastructure Grants, ARC LIEF, NCRIS/AuScope, industry partners, and Macquarie University.

SUPPLEMENTARY DATA

Supplementary data are available at *Journal of Petrology* online.

References

Alt, J. C., Zuleger, E. & Erzinger, J. (1995) Mineralogy and stable isotopic compositions of the hydrothermally altered lower sheeted dike complex, Hole 504B, Leg 140. In: (Erzinger J., Becker K., Dick H. J. B. & Stokking L. B. (eds)) *Proceedings of the Ocean Drilling Program, Scientific Results*, vol. 137. College Station, TX: Ocean Drilling Program, pp.155–166.

Alt, J. C., Laverne, C., Coggon, R. M., Teagle, D. A. H., Banerjee, N. R., Morgan, S., Smith-Duque, C. E., Harris, M. & Galli, L. (2010). Subsurface structure of a submarine hydrothermal system in ocean crust formed at the East Pacific Rise, ODP/IODP site 1256. *Geochemistry, Geophysics, Geosystems* **11**, 28.

Andrews, G., Harris, P. D., Brown, S., Anderson, L. & Moreno, N. (2014) *A New Sample Transect through the Sierra Madre Occidental Silicic Large Igneous Province in Southern Chihuahua State, Mexico: First Stratigraphic, Petrologic, and Geochemical Results*. AGU Fall meeting. San Francisco: American Geophysical Union (AGU), pp.V33B–V4860B.

Arnulf, A. F., Harding, A. J., Kent, G. M., Carbotte, S. M., Canales, J. P. & Nedimović, M. R. (2014). Anatomy of an active submarine volcano. *Geology* **42**, 655–658.

Ashwal, L. D., Wiedenbeck, M. & Torsvik, T. H. (2017). Archaean zircons in Miocene oceanic hotspot rocks establish ancient continental crust beneath Mauritius. *Nature Communications* **8**, 14086.

Barth, A. P., Tani, K., Meffre, S., Wooden, J. L., Coble, M. A., Arculus, R. J., Ishizuka, O. & Shukle, J. T. (2017). Generation of silicic melts in the early Izu–Bonin arc recorded by detrital zircons in proximal arc volcaniclastic rocks from the Philippine Sea. *Geochemistry, Geophysics, Geosystems* **18**, 3576–3591.

Beier, C., Bach, W., Turner, S., Niedermeier, D., Woodhead, J., Erzinger, J. & r. & Krumm, S. (2015). Origin of silicic magmas at spreading centres—an example from the South East Rift, Manus Basin. *Journal of Petrology* **56**, 255–272.

Berndt, J., Koepke, J. & Holtz, F. O. (2004). An experimental investigation of the influence of water and oxygen fugacity on differentiation of MORB at 200 MPa. *Journal of Petrology* **46**, 135–167.

Bindeman, I. (2008). Oxygen isotopes in mantle and crustal magmas as revealed by single crystal analysis. *Reviews in Mineralogy and Geochemistry* **69**, 445–478.

Bindeman, I., Gurenko, A., Carley, T., Miller, C., Martin, E. & Sigmarsson, O. (2012a). Silicic magma petrogenesis in Iceland by remelting of hydrothermally altered crust based on oxygen isotope diversity and disequilibria between zircon and magma with implications for MORB. *Terra Nova* **24**, 227–232.

Bindeman, I. N., Kamenetsky, V. S., Palandri, J. & Vennemann, T. (2012b). Hydrogen and oxygen isotope behaviors during variable

degrees of upper mantle melting: example from the basaltic glasses from Macquarie Island. *Chemical Geology* **310–311**, 126–136.

Blichert-Toft, J. & White, W. M. (2001). Hf isotope geochemistry of the Galapagos Islands. *Geochemistry, Geophysics, Geosystems* **2**, 20.

Bouvier, A., Vervoort, J. D. & Patchett, P. J. (2008). The Lu-Hf and Sm-Nd isotopic composition of CHUR: constraints from un-equilibrated chondrites and implications for the bulk composition of terrestrial planets. *Earth and Planetary Science Letters* **273**, 48–57.

Brophy, J. G. (2009). La-SiO2 and Yb-SiO_2 systematics in mid-ocean ridge magmas: implications for the origin of oceanic plagiogranite. *Contributions to Mineralogy and Petrology* **158**, 99–111.

Bucholz, C. E., Jagoutz, O., VanTongeren, J. A., Setera, J. & Wang, Z. (2017). Oxygen isotope trajectories of crystallizing melts: insights from modeling and the plutonic record. *Geochimica et Cosmochimica Acta* **207**, 154–184.

Buck, W. R., Lavier, L. L. & Poliakov, A. N. B. (2005). Modes of faulting at mid-ocean ridges. *Nature* **434**, 719–723.

Byerly, G. (1980). The nature of differentiation trends in some volcanic rocks from the Galapagos spreading center. *Journal of Geophysical Research: Solid Earth* **85**, 3797–3810.

Carley, T. L., Miller, C. F., Wooden, J. L., Padilla, A. J., Schmitt, A. K., Economos, R. C., Bindeman, I. N. & Jordan, B. T. (2014). Iceland is not a magmatic analog for the Hadean: evidence from the zircon record. *Earth and Planetary Science Letters* **405**, 85–97.

Castillo, P. R., Hawkins, J. W., Lonsdale, P. F., Hilton, D. R., Shaw, A. M. & Glascock, M. D. (2002). Petrology of Alarcon Rise lavas, Gulf of California: nascent intracontinental ocean crust. *Journal of Geophysical Research: Solid Earth* **107**, ECV 5-1–ECV 5-15.

Charlier, B., Namur, O. & Grove, T. L. (2013). Compositional and kinetic controls on liquid immiscibility in ferrobasalt-rhyolite volcanic and plutonic series. *Geochimica et Cosmochimica Acta* **113**, 79–93.

Christie, D. M. & Sinton, J. M. (1981). Evolution of abyssal lavas along propagating segments of the Galapagos spreading center. *Earth and Planetary Science Letters* **56**, 321–335.

Clague, D. A., Caress, D. W., Dreyer, B. M., Lundsten, L., Paduan, J. B., Portner, R. A., Spelz-Madero, R., Bowles, J. A., Castillo, P. R., Guardado-France, R., Le Saout, M., Martin, J. F., Santa Rosa-del Río, M. A. & Zierenberg, R. A. (2018). Geology of the Alarcon Rise, southern Gulf of California. *Geochemistry, Geophysics, Geosystems* **19**, 565–976.

Claiborne, L. L., Miller, C. F., Walker, B. A., Wooden, J. L., Mazdab, F. K. & Bea, F. (2006). Tracking magmatic processes through Zr/Hf ratios in rocks and Hf and Ti zoning in zircons: an example from the Spirit Mountain batholith, Nevada. *Mineralogical Magazine* **70**, 517–543.

Clog, M., Aubaud, C., Cartigny, P. & Dosso, L. (2013). The hydrogen isotopic composition and water content of southern Pacific MORB: a reassessment of the D/H ratio of the depleted mantle reservoir. *Earth and Planetary Science Letters* **381**, 156–165.

Coumou, D., Driesner, T., Weis, P. & Heinrich, C. A. (2009). Phase separation, brine formation, and salinity variation at black smoker hydrothermal systems. *Journal of Geophysical Research: Solid Earth* **114**, 16.

De Bievre, P. & Taylor, P. D. P. (1993). Table of the isotopic compositions of the elements. *International Journal of Mass Spectrometry and Ion Processes* **123**, 149–166.

Deardorff, N. D., Cashman, K. V. & Chadwick, W. W., J. (2011). Observations of eruptive plume dynamics and pyroclastic deposits from submarine explosive eruptions at NW Rota-1, Mariana arc. *Journal of Volcanology and Geothermal Research* **202**, 47–59.

DeMets, C., Gordon, R. G. & Argus, D. F. (2010). Geologically current plate motions. *Geophysical Journal International* **181**, 1–80.

Dixon, S. & Rutherford, M. J. (1979). Plagiogranites as late-stage immiscible liquids in ophiolite and mid-ocean ridge suites: an experimental study. *Earth and Planetary Science Letters* **45**, 45–60.

Dixon, J. E., Bindeman, I. N., Kingsley, R. H., Simons, K. K., Le Roux, P. J., Hajewski, T. R., Swart, P., Langmuir, C. H., Ryan, J. G., Walowski, K. J., Wada, I. & Wallace, P. J. (2017). Light stable isotopic compositions of enriched mantle sources: resolving the dehydration paradox. *Geochemistry, Geophysics, Geosystems* **18**, 3801–3839.

Dreyer, B., Portner, R. A., Clague, D., Daczko, N., Castillo, P. R. & Bindeman, I. N. (2014) *Mineral Chemistry of Silica-Rich Lavas, Alarcon Rise (EPR)*. AGU Fall meeting. San Francisco: American Geophysical Union (AGU), pp.V31B–V4746B.

Ersoy, Y. & Helvaci, C. (2010). FC-AFC-FCA and mixing modeler: a Microsoft® Excel© spreadsheet program for modeling geochemical differentiation of magma by crystal fractionation, crustal assimilation and mixing. *Computers & Geosciences* **36**, 383–390.

Etheridge, M. A., Daczko, N. R., Chapman, T. & Stuart, C. A. (2020). Mechanisms of melt extraction during lower crustal partial melting. *Journal of Metamorphic Geology* **39**, 57–75.

Ferrari, L., Valencia-Moreno, M. & n. & Bryan, S. (2007). Magmatism and tectonics of the Sierra Madre Occidental and its relation with the evolution of the western margin of North America. *Geological Society of America Special Papers* **422**, 1–39.

Ferry, J. M. & Watson, E. B. (2007). New thermodynamic models and revised calibrations for the Ti-in-zircon and Zr-in-rutile thermometers. *Contributions to Mineralogy and Petrology* **154**, 429–437.

Fisher, C. M., Vervoort, J. D. & Hanchar, J. M. (2014). Guidelines for reporting zircon Hf isotopic data by LA-MC-ICPMS and potential pitfalls in the interpretation of these data. *Chemical Geology* **363**, 125–133.

Fletcher, J. M., Grove, M., Kimbrough, D., Lovera, O. & Gehrels, G. E. (2007). Ridge-trench interactions and the Neogene tectonic evolution of the Magdalena shelf and southern Gulf of California: insights from detrital zircon U-Pb ages from the Magdalena fan and adjacent areas. *Geological Society of America Bulletin* **119**, 1313–1336.

France, L., Koepke, J., Ildefonse, B., Cichy, S. B. & Deschamps, F. (2010). Hydrous partial melting in the sheeted dike complex at fast spreading ridges: experimental and natural observations. *Contributions to Mineralogy and Petrology* **160**, 683–704.

Gain, S. E. M., Gréau, Y., Henry, H., Belousova, E., Dainis, I., Griffin, W. L. & O'Reilly, S. Y. (2019). Mud tank zircon: long-term evaluation of a reference material for U-Pb dating, Hf-isotope analysis and trace element analysis. *Geostandards and Geoanalytical Research* **43**, 339–354.

Geist, D., Howard, K. A. & Larson, P. (1995). The generation of oceanic rhyolites by crystal fractionation: the basalt-rhyolite Association at Volcan Alcedo, Galapagos archipelago. *Journal of Petrology* **36**, 965–982.

Gerlach, D., Leeman, W. & Ave Lallemant, H. (1981). Petrology and geochemistry of plagiogranite in the Canyon Mountain ophiolite, Oregon. *Contributions to Mineralogy and Petrology* **77**, 82–92.

Gillis, K. M. (1995). Controls on hydrothermal alteration in a section of fast-spreading oceanic crust. *Earth and Planetary Science Letters* **134**, 473–489.

Griffin, W. L., Pearson, N. J., Belousova, E., Jackson, S. E., van Achterbergh, E., O'Reilly, S. Y. & Shee, S. R. (2000). The Hf isotope composition of cratonic mantle; LAM-MC-ICPMS analysis of zircon megacrysts in kimberlites. *Geochimica et Cosmochimica Acta* **64**, 133–147.

Griffin, W. L., Wang, X., Jackson, S. E., Pearson, N. J., O'Reilly, S. Y., Xu, X. & Zhou, X. (2002). Zircon chemistry and magma mixing, SE

China: *in-situ* analysis of Hf isotopes, Tonglu and Pingtan igneous complexes. *Lithos* **61**, 237–269.

Grimes, C. B., John, B. E., Kelemen, P. B., Mazdab, F. K., Wooden, J. L., Cheadle, M. J., Hanghoj, K. & Schwartz, J. J. (2007). Trace element chemistry of zircons from oceanic crust: a method for distinguishing detrital zircon provenance. *Geology* **35**, 643–646.

Grimes, C. B., John, B. E., Cheadle, M. J., Mazdab, F. K., Wooden, J. L., Swapp, S. & Schwartz, J. J. (2009). On the occurrence, trace element geochemistry, and crystallization history of zircon from *in situ* ocean lithosphere. *Contributions to Mineralogy and Petrology* **158**, 757–783.

Grimes, C. B., Ushikubo, T., John, B. E. & Valley, J. W. (2011). Uniformly mantle-like $\delta^{18}O$ in zircons from oceanic plagiogranites and gabbros. *Contributions to Mineralogy and Petrology* **161**, 13–33.

Grimes, C. B., Ushikubo, T., Kozdon, R. & Valley, J. W. (2013). Perspectives on the origin of plagiogranite in ophiolites from oxygen isotopes in zircon. *Lithos* **179**, 48–66.

Grimes, C. B., Wooden, J. L., Cheadle, M. J. & John, B. E. (2015). "Fingerprinting" tectono-magmatic provenance using trace elements in igneous zircon. *Contributions to Mineralogy and Petrology* **170**, 1–26.

Gualda, G. A. R., Ghiorso, M. S., Lemons, R. V. & Carley, T. L. (2012). Rhyolite-MELTS: a modified calibration of MELTS optimized for silica-rich, fluid-bearing magmatic systems. *Journal of Petrology* **53**, 875–890.

Haase, K. M., Stroncik, N. A., Hekinian, R. & Stoffers, P. (2005). Nb-depleted andesites from the Pacific-Antarctic Rise as analogs for early continental crust. *Geology* **33**, 921–924.

Halpin, J. A., Daczko, N. R., Direen, N. G., Mulder, J. A., Murphy, R. C. & Ishihara, T. (2020). Provenance of rifted continental crust at the nexus of East Gondwana breakup. *Lithos* **354–355**, 105363.

Hampton, R. L., Bindeman, I. N., Stern, R. A., Coble, M. A. & Rooyakkers, S. M. (2021). A microanalytical oxygen isotopic and U-Th geochronologic investigation and modeling of rhyolite petrogenesis at the Krafla central volcano, Iceland. *Journal of Volcanology and Geothermal Research* **414**, 107229.

Hoskin, P. W. O. (2005). Trace-element composition of hydrothermal zircon and the alteration of Hadean zircon from the Jack Hills, Australia. *Geochimica et Cosmochimica Acta* **69**, 637–648.

Huang, H., Niu, Y., Teng, F.-Z. & Wang, S.-J. (2019). Discrepancy between bulk-rock and zircon Hf isotopes accompanying Nd-Hf isotope decoupling. *Geochimica et Cosmochimica Acta* **259**, 17–36.

Ito, G. & Behn, M. D. (2008). Magmatic and tectonic extension at mid-ocean ridges: 2. Origin of axial morphology. *Geochemistry, Geophysics, Geosystems* **9**.

Jackson, S. E., Pearson, N. J., Griffin, W. L. & Belousova, E. A. (2004). The application of laser ablation-inductively coupled plasma-mass spectrometry to in situ U-Pb zircon geochronology. *Chemical Geology* **211**, 47–69.

Jeanvoine, A., Chazot, G., Labanieh, S., Pelleter, E. & Fouquet, Y. (2021). Origin and evolution of the Fatu Kapa magmatic system (North-Western Lau Back-Arc Basin): insight on the genesis of high-silica lavas. *Journal of Petrology* **62**, 1–33.

Jeffcoat, C. R. (2012). Uranium-lead zircon geochronology, hafnium isotope and trace element geochemistry of a unique lower crustal—upper mantle section of a dying slow-spreading mid-ocean ridge (Macquarie Island, Southern Ocean). Unpublished M.S. thesis, University of Alabama. 96.

Jöns, N., Bach, W. & Schroeder, T. (2009). Formation and alteration of plagiogranites in an ultramafic-hosted detachment fault at the mid-Atlantic ridge (ODP leg 209). *Contributions to Mineralogy and Petrology* **157**, 625–639.

Juster, T. C., Grove, T. L. & Perfit, M. R. (1989). Experimental constraints on the generation of FeTi basalts, andesites, and rhyodacites at the Galapagos Spreading Center, 85°W and 95°W. *Journal of Geophysical Research: Solid Earth* **94**, 9251–9274.

Keigwin, L. D. (2002). Late Pleistocene-Holocene paleoceanography and ventilation of the Gulf of California. *Journal of Oceanography* **58**, 421–432.

Kelley, D. S. & Früh-Green, G. L. (2001). Volatile lines of descent in submarine plutonic environments: insights from stable isotope and fluid inclusion analyses. *Geochimica et Cosmochimica Acta* **65**, 3325–3346.

Kemp, A. I. S., Hawkesworth, C. J., Foster, G. L., Paterson, B. A., Woodhead, J. D., Hergt, J. M., Gray, C. M. & Whitehouse, M. J. (2007). Magmatic and crustal differentiation history of granitic rocks from Hf-O isotopes in zircon. *Science* **315**, 980–983.

Kendrick, M. A., Arculus, R., Burnard, P. & Honda, M. (2013). Quantifying brine assimilation by submarine magmas: examples from the Galapagos Spreading Centre and Lau Basin. *Geochimica et Cosmochimica Acta* **123**, 150–165.

Kent, A. J. R., Norman, M. D., Hutcheon, I. D. & Stolper, E. M. (1999). Assimilation of seawater-derived components in an oceanic volcano: evidence from matrix glasses and glass inclusions from Loihi seamount, Hawaii. *Chemical Geology* **156**, 299–319.

Kita, N. T., Ushikubo, T., Fu, B. & Valley, J. W. (2009). High precision SIMS oxygen isotope analysis and the effect of sample topography. *Chemical Geology* **264**, 43–57.

Koepke, J., Feig, S., Snow, J. & Freise, M. (2004). Petrogenesis of oceanic plagiogranites by partial melting of gabbros: an experimental study. *Contributions to Mineralogy and Petrology* **146**, 414–432.

Koepke, J., Berndt, J., Feig, S. T. & Holtz, F. (2007). The formation of SiO_2-rich melts within the deep oceanic crust by hydrous partial melting of gabbros. *Contributions to Mineralogy and Petrology* **153**, 67–84.

Kostitsyn, Y. A., Belousova, E. A., Bortnikov, N. S. & Sharkov, E. V. (2009). Zircons in gabbroids from the axial zone of the mid-Atlantic ridge: U-Pb age and 176Hf/177Hf ratio (results of investigations by the laser ablation method). *Doklady Earth Sciences* **429**, 1305–1309.

Le Saout, M., Clague, D. A. & Paduan, J. B. (2019). Evolution of fine-scale segmentation at intermediate-spreading rate ridges. *Geochemistry, Geophysics, Geosystems* **20**, 3841–3860.

Lee, C.-T. A. & Morton, D. M. (2015). High silica granites: terminal porosity and crystal settling in shallow magma chambers. *Earth and Planetary Science Letters* **409**, 23–31.

Lee, C.-T. A., Morton, D. M., Farner, M. J. & Moitra, P. (2015). Field and model constraints on silicic melt segregation by compaction/hindered settling: the role of water and its effect on latent heat release. *American Mineralogist* **100**, 1762–1777.

Lizarralde, D., Axen, G. J., Brown, H. E., Fletcher, J. M., Gonzalez-Fernandez, A., Harding, A. J., Holbrook, W. S., Kent, G. M., Paramo, P., Sutherland, F. & Umhoefer, P. J. (2007). Variation in styles of rifting in the Gulf of California. *Nature* **448**, 466–469.

Manga, M. (1996). Mixing of heterogeneities in the mantle: effect of viscosity differences. *Geophysical Research Letters* **23**, 403–406.

Martin, E., Bindeman, I., Balan, E., Palandri, J., Seligman, A. & Villemant, B. (2017). Hydrogen isotope determination by TC/EA technique in application to volcanic glass as a window into secondary hydration. *Journal of Volcanology and Geothermal Research* **348**, 49–61.

Michael, P. J. & Cornell, W. C. (1998). Influence of spreading rate and magma supply on crystallization and assimilation beneath mid-ocean ridges: evidence from chlorine and major element chemistry of mid-ocean ridge basalts. *Journal of Geophysical Research: Solid Earth* **103**, 18325–18356.

Michael, P. J. & Schilling, J.-G. (1989). Chlorine in mid-ocean ridge magmas: evidence for assimilation of seawater-influenced components. *Geochimica et Cosmochimica Acta* **53**, 3131–3143.

Morag, N., Golan, T., Katzir, Y., Coble, M. A., Kitajima, K. & Valley, J. W. (2020). The origin of plagiogranites: coupled SIMS O isotope ratios, U-Pb dating and trace element composition of zircon from the Troodos Ophiolite, Cyprus. *Journal of Petrology* **61**, 18.

Muehlenbachs, K. & Byerly, G. (1982). 18O-Enrichment of silicic magmas caused by crystal fractionation at the Galapagos Spreading Center. *Contributions to Mineralogy and Petrology* **79**, 76–79.

Munker, C., Weyer, S., Scherer, E. & Mezger, K. (2001). Separation of high field strength elements (Nb, Ta, Zr, Hf) and Lu from rock samples for MC-ICPMS measurements. *Geochemistry, Geophysics, Geosystems* **2**, 19.

Nardi, L. V. S., Formoso, M. L. L., Muller, I. F., Fontana, E., Jarvis, K. & Lamarao, C. (2013). Zircon/rock partition coefficients of REEs, Y, Th, U, Nb, and Ta in granitic rocks: uses for provenance and mineral exploration purposes. *Chemical Geology* **335**, 1–7.

Nehlig, P. (1991). Salinity of oceanic hydrothermal fluids: a fluid inclusion study. *Earth and Planetary Science Letters* **102**, 310–325.

Newman, S. & Lowenstern, J. B. (2002). VolatileCalc: a silicate melt-H_2O-CO_2 solution model written in Visual Basic for Excel. *Computers & Geosciences* **28**, 597–604.

Nicholson, H., Condomines, M., Fitton, J. G., Fallick, A. E., Gronvold, K. & Rogers, G. (1991). Geochemical and isotopic evidence for crustal assimilation beneath Krafla, Iceland. *Journal of Petrology* **32**, 1005–1020.

Nowell, G. M., Kempton, P. D., Noble, S. R., Fitton, J. G., Saunders, A. D., Mahoney, J. J. & Taylor, R. N. (1998). High precision Hf isotope measurements of MORB and OIB by thermal ionization mass spectrometry: insights into the depleted mantle. *Chemical Geology* **149**, 211–233.

Oskarsson, N., Sigvaldason, G. E. & Steinthorsson, S. (1982). A dynamic model of rift zone petrogenesis and the regional petrology of Iceland. *Journal of Petrology* **23**, 28–74.

Padilla, A. J., Miller, C. F., Carley, T. L., Economos, R. C., Schmitt, A. K., Coble, M. A., Wooden, J. L., Fisher, C. M., Vervoort, J. D. & Hanchar, J. M. (2016). Elucidating the magmatic history of the Austurhorn silicic intrusive complex (Southeast Iceland) using zircon elemental and isotopic geochemistry and geochronology. *Contributions to Mineralogy and Petrology* **171**, 1–21.

Pedersen, R. & Malpas, J. (1984). The origin of oceanic plagiogranites from the Karmoy ophiolite, western Norway. *Contributions to Mineralogy and Petrology* **88**, 36–52.

Perfit, M. R., Fornari, D. J., Malahoff, A. & Embley, R. W. (1983). Geochemical studies of abyssal lavas recovered by DSRV Alvin from eastern Galapagos Rift, Inca Transform, and Ecuador Rift: 3. Trace element abundances and petrogenesis. *Journal of Geophysical Research: Solid Earth* **88**, 10551–10572.

Perfit, M. R., Ridley, W. I. & Jonasson, I. R. (1999). Geologic, petrologic and geochemical relationships between magmatism and massive sulfide mineralization along the eastern Galapagos Spreading Center. *Reviews in Economic Geology* **8**, 75–100.

Perfit, M. R., Cann, J. R., Fornari, D. J., Engels, J., Smith, D. K., Ian Ridley, W. & Edwards, M. H. (2003). Interaction of sea water and lava during submarine eruptions at mid-ocean ridges. *Nature* **426**, 62–65.

Pietranik, A., Storey, C., Koepke, J. & Lasalle, S. (2017). Zircon record of fractionation, hydrous partial melting and thermal gradients at different depths in oceanic crust (ODP site 735B, south-west Indian Ocean). *Contributions to Mineralogy and Petrology* **172**, 10.

Portner, R. A., Daczko, N. R., Murphy, M. J. & Pearson, N. J. (2011). Enriching mantle melts within a dying mid-ocean spreading ridge: insights from Hf-isotope and trace element patterns in detrital oceanic zircon. *Lithos* **126**, 355–368.

Portner, R., Clague, D. & Paduan, J. (2014). Caldera formation and varied eruption styles on North Pacific seamounts: the clastic lithofacies record. *Bulletin of Volcanology* **76**, 28.

Portner, R. A., Dreyer, B. M., Clague, D. A., Spelz, R. M., Lowenstern, J. B., Paduan, J. B. & Carey, S. (2015) Rhyolite eruption on a mid-ocean ridge: Alarcon Rise, Gulf of California. In: *GSA Annual Meeting, abstract 145-5*. Baltimore: Geological Society of America (GSA).

Portner, R. A., Dreyer, B. M. & Clague, D. A. (2021). Mid-ocean-ridge rhyolite (MORR) eruptions on the East Pacific Rise lack the fizz to pop. *Geology* **49**, 377–381.

le Roux, P. J., Shirey, S. B., Hauri, E. H., Perfit, M. R. & Bender, J. F. (2006). The effects of variable sources, processes and contaminants on the composition of northern EPR MORB (8°10 N and 12°14 N): evidence from volatiles (H_2O, CO_2, S) and halogens (F, Cl). *Earth and Planetary Science Letters* **251**, 209–231.

Salters, V. J. M., Mallick, S., Hart, S. R., Langmuir, C. E. & Stracke, A. (2011). Domains of depleted mantle: new evidence from hafnium and neodymium isotopes. *Geochemistry, Geophysics, Geosystems* **12**, 18.

Schaaf, P., Böhnel, H. & Pérez-Venzor, J. A. (2000). Pre-Miocene palaeogeography of the Los Cabos block, Baja California Sur: geochronological and palaeomagnetic constraints. *Tectonophysics* **318**, 53–69.

Scherer, E., Munker, C. & Mezger, K. (2001). Calibration of the lutetium-hafnium clock. *Science* **293**, 683–687.

Schmitt, A. K., Perfit, M. R., Rubin, K. H., Stockli, D. F., Smith, M. C., Cotsonika, L. A., Zellmer, G. F., Ridley, W. I. & Lovera, O. M. (2011). Rapid cooling rates at an active mid-ocean ridge from zircon thermochronology. *Earth and Planetary Science Letters* **302**, 349–358.

Schwartz, J. J., John, B. E., Cheadle, M. J., Miranda, E. A., Grimes, C. B., Wooden, J. L. & Dick, H. J. B. (2005). Dating the growth of oceanic crust at a slow-spreading ridge. *Science* **310**, 654–657.

Sharapov, V. N., Tomilenko, A. A., Smirnov, S. Z., Sharygin, V. V. & Kovyazin, S. V. (2013). Rhyolite xenolith from the neovolcanic basalts of the rift valley of the Juan de Fuca Ridge, northeastern pacific: reconstruction of crystallization conditions and interaction between MOR silicic rocks and basic magmas. *Petrology* **21**, 427–453.

Shaw, S. E. & Flood, R. H. (2009). Zircon Hf isotopic evidence for mixing of crustal and silicic mantle-derived magmas in a zoned granite pluton, eastern Australia. *Journal of Petrology* **50**, 147–168.

Sheppard, S. F. & Harris, C. (1985). Hydrogen and oxygen isotope geochemistry of Ascension Island lavas and granites: variation with crystal fractionation and interaction with sea water. *Contributions to Mineralogy and Petrology* **91**, 74–81.

Sinton, J., Bergmanis, E., Rubin, K., Batiza, R., Gregg, T. K. P., Gronvold, K., Macdonald, K. C. & White, S. M. (2002). Volcanic eruptions on mid-ocean ridges: new evidence from the superfast spreading East Pacific Rise, 17°–19°S. *Journal of Geophysical Research: Solid Earth* **107**, 20.

Sparks, J. W. (1995) Geochemistry of the lower sheeted dike complex, Hole 504B, Leg 140. In: (Erzinger J., Becker K., Dick H. J. B. & Stokking L. B. (eds)) *Proceedings of the Ocean Drilling Program, Scientific Results*, vol. 137. College Station, TX: Ocean Drilling Program, pp. 81–97.

Sun, S. & McDonough, W. F. (1989). Chemical and isotopic systematics of oceanic basalts: implications for mantle composition and processes. *Geological Society, London, Special Publications* **42**, 313–345.

Sutherland, F. H. (2006). Continental rifting across the southern Gulf of California. Unpublished Ph.D. thesis 189, University of California San Diego.

Tang, M., Wang, X.-L., Shu, X.-J., Wang, D., Yang, T. & Gopon, P. (2014). Hafnium isotopic heterogeneity in zircons from granitic rocks: geochemical evaluation and modeling of "zircon effect" in crustal anatexis. *Earth and Planetary Science Letters* **389**, 188–199.

Thomas, C. L. (2013) *Hafnium Isotope Geochemistry of the Gabbroic Crust Sampled Along the Mid-Atlantic Ridge: Constraints on the Nature of the Upper Mantle*. Athens, Ohio, USA: Ohio University.

Valley, J. W. (2003). Oxygen isotopes in zircon. *Reviews in Mineralogy and Geochemistry* **53**, 343–385.

Valley, J. W., Lackey, J. S., Cavosie, A. J., Clechenko, C. C., Spicuzza, M. J., Basei, M. A. S., Bindeman, I. N., Ferreira, V. P., Sial, A. N., King, E. M., Peck, W. H., Sinha, A. K. & Wei, C. S. (2005). 4.4 billion years of crustal maturation: oxygen isotope ratios of magmatic zircon. *Contributions to Mineralogy and Petrology* **150**, 561–580.

Van Der Zander, I., Sinton, J. M. & Mahoney, J. J. (2010). Late shield-stage silicic magmatism at Wai'anae volcano: evidence for hydrous crustal melting in Hawaiian volcanoes. *Journal of Petrology* **51**, 671–701.

Vermeesch, P. (2018). IsoplotR: a free and open toolbox for geochronology. *Geoscience Frontiers* **9**, 1479–1493.

Vervoort, J. D., Plank, T. & Prytulak, J. (2011). The Hf-Nd isotopic composition of marine sediments. *Geochimica et Cosmochimica Acta* **75**, 5903–5926.

Vigneresse, J. L., Barbey, P. & Cuney, M. (1996). Rheological transitions during partial melting and crystallization with application to felsic magma segregation and transfer. *Journal of Petrology* **37**, 1579–1600.

Wanless, V. D., Perfit, M. R., Ridley, W. I. & Klein, E. (2010). Dacite petrogenesis on mid-ocean ridges: evidence for oceanic crustal melting and assimilation. *Journal of Petrology* **51**, 2377–2410.

Wanless, V. D., Perfit, M. R., Ridley, W. I., Wallace, P. J., Grimes, C. B. & Klein, E. M. (2011). Volatile abundances and oxygen isotopes in basaltic to dacitic lavas on mid-ocean ridges: the role of assimilation at spreading centers. *Chemical Geology* **287**, 54–65.

White, S. M., Crisp, J. A. & Spera, F. J. (2006). Long-term volumetric eruption rates and magma budgets. *Geochemistry, Geophysics, Geosystems* **7**, 20.

Wiedenbeck, M., Hanchar, J. M., Peck, W. H., Sylvester, P., Valley, J., Whitehouse, M., Kronz, A., Morishita, Y., Nasdala, L., Fiebig, J., Franchi, I., Girard, J. P., Greenwood, R. C., Hinton, R., Kita, N., Mason, P. R. D., Norman, M., Ogasawara, M., Piccoli, P. M., Rhede, D., Satoh, H., Schulz-Dobrick, B., Skår, O., Spicuzza, M. J., Terada, K., Tindle, A., Togashi, S., Vennemann, T., Xie, Q. & Zheng, Y. F. (2004). Further characterisation of the 91500 zircon crystal. *Geostandards and Geoanalytical Research* **28**, 9–39.

Woodhead, J. D. & Hergt, J. M. (2005). A preliminary appraisal of seven natural zircon reference materials for in situ Hf isotope determination. *Geostandards and Geoanalytical Research* **29**, 183–195.

Workman, R. K. & Hart, S. R. (2005). Major and trace element composition of the depleted MORB mantle (DMM). *Earth and Planetary Science Letters* **231**, 53–72.

Wu, F.-Y., Yang, Y.-H., Xie, L.-W., Yang, J.-H. & Hu, P. (2006). Hf isotopic compositions of the standard zircons and baddeleyites used in U-Pb geochronology. *Chemical Geology* **234**, 105–126.

Yang, J.-H., Wu, F.-Y., Wilde, S. A., Xie, L.-W., Yang, Y.-H. & Liu, X.-M. (2007). Tracing magma mixing in granite genesis: in situ U-Pb dating and Hf-isotope analysis of zircons. *Contributions to Mineralogy and Petrology* **153**, 177–190.

Zhang, Y., Meng, F. & Niu, Y. (2016). Hf isotope systematics of seamounts near the East Pacific Rise (EPR) and geodynamic implications. *Lithos* **262**, 107–119.

Zuleger, E., Alt, J. C. & Erzinger, J. (1995) Primary and secondary variations in major and trace element geochemistry of the lower sheeted dike complex: Hole 504B, Leg 140. In: (Erzinger J., Becker K., Dick H. J. B. & Stokking L. B. (eds)) *Proceedings of the Ocean Drilling Program, Scientific Results*, vol. 137. College Station, TX: Ocean Drilling Program, pp. 65–80.